The actomyosin system is essential for the integrity of the endosomal system in bloodstream form *Trypanosoma brucei*

Running title: The actomyosin system of bloodstream form *Trypanosoma brucei*.

Authors:

Fabian Link[1], Sisco Jung*[1], Xenia Malzer*[1], Felix Zierhut[2,3], Antonia Konle[1], Alyssa Borges[1], Christopher Batters[2,3], Monika Weiland[1], Mara Pöllmann[1], An Binh Nguyen[1], Johannes Kullmann[1], Claudia Veigel[2,3], Markus Engstler[1], Brooke Morriswood[1]

* These authors contributed equally.

Affiliations:

[1]Department of Cell & Developmental Biology, Biocenter, University of Würzburg, Am Hubland, 97074 Würzburg, Germany

[2]Ludwig-Maximilians-Universität München, Department of Cellular Physiology, Biomedical Centre (BMC) Grosshadnerstraße 9, 82152 Planegg-Martinsried, Germany

[3]Center for Nanosciences (CeNS), Schellingstraße 4, 80799 München, Germany

Corresponding authors: Markus Engstler (markus.engstler@biozentrum.uni-wuerzburg.de), Brooke Morriswood (brooke.morriswood@gmail.com)

Keywords:

Myosin, actin, TbMyo1, TbMyo21, chromobody, endosomes, TbRab proteins

Abstract

The actin cytoskeleton is a ubiquitous feature of eukaryotic cells, yet its complexity varies across different taxa. In the parasitic protist *Trypanosoma brucei*, a rudimentary actomyosin system consisting of one actin gene and two myosin genes has been retained despite significant investment in the microtubule cytoskeleton. The functions of this highly simplified actomyosin system remain unclear, but appear to centre on the endomembrane system. Here, advanced light and electron microscopy imaging techniques together with biochemical and biophysical assays were used to explore the relationship between the actomyosin and endomembrane systems. The class I myosin (TbMyo1) had a large cytosolic pool and its ability to translocate actin filaments *in vitro* was shown here for the first time. TbMyo1 exhibited strong association with the endosomal system and was additionally found on glycosomes. At the endosomal membranes, TbMyo1 colocalised with markers for early and late endosomes (TbRab5A and TbRab7, respectively), but not with the marker associated with recycling endosomes (TbRab11). Actin and myosin were simultaneously visualised for the first time in trypanosomes using an anti-actin chromobody. Disruption of the actomyosin system using the actin-depolymerising drug latrunculin A resulted in a delocalisation of both the actin chromobody signal and an endosomal marker, and was accompanied by a specific loss of endosomal structure. This suggests that the actomyosin system is required for maintaining endosomal integrity in *T. brucei*.

Introduction

The actin cytoskeleton is a universal feature of eukaryotic cells and plays critical roles in processes such as endocytosis, cytokinesis, and maintenance of cell morphology. Most research has however focused on opisthokonts (principally animals and fungi), and very little is known about the actomyosin system in other branches of the eukaryotic tree, in particular the early-branching ones. Recently, it was shown that trypanosomatids – a family of unicellular parasites – are the most divergent eukaryotes that still retain an actomyosin system with associated regulatory proteins (Kotila et al., 2022). Amongst the trypanosomatids, *Trypanosoma brucei* is the most tractable for molecular cell biology investigation. *T. brucei* is an exclusively extracellular pathogen which has evolved mechanisms to resist the harsh conditions within the bloodstream and body fluids of its mammalian hosts and the different but similarly demanding environments within its insect vector, the tsetse fly.

To evade the mammalian host's immune system, *T. brucei* bloodstream forms (BSFs) express a surface coat of variable surface glycoproteins (VSGs) consisting of 5 x 10^6 VSG dimers (Bartossek et al., 2017; Cross, 1975; Jackson et al., 1985). This dense glycoprotein coat hides invariant surface proteins from immune recognition, ensuring that host antibodies are generated against the currently-presented VSG isoform and not against any invariant surface proteins (Cross, 1975; Mugnier et al., 2016). A glycosylphosphatidylinositol (GPI) anchor attached to each VSG monomer confers high mobility to the VSG coat, facilitating a high rate of antibody clearance by the parasite (Bartossek et al., 2017; Borges et al., 2021; Hartel et al., 2016). The directional movement of the trypanosome generates hydrodynamic flow forces on the cell surface that drag VSG-antibody complexes to the posterior region of the cell, where they can be endocytosed, trafficked to the lysosome, and degraded (Engstler et al., 2007; Link et al., 2021; Webster et al., 1990). Thus, *T. brucei* persistence inside the mammalian host is intrinsically connected to its endocytic trafficking capacity.

All endo- and exocytic processes in *T. brucei* occur through the flagellar pocket, a small invagination of the plasma membrane located near the posterior pole of the cell (Grünfelder et al., 2002; Grünfelder et al., 2003; Lacomble et al., 2009). Measurements of the kinetics of VSG endocytosis and recycling revealed that the VSG cell surface pool is turned over within 12 minutes (Engstler et al., 2004). Surface-bound antibodies are internalised and colocalise with lysosome markers within 2 minutes (Engstler et al., 2007). These rates are very high, especially considering that exo- and endocytosis are limited to only 5% of the total cell surface area (Engstler et al., 2004). Moreover, not only is the flagellar pocket situated in the posterior part

78 of the cell, but the entire endosomal apparatus responsible for membrane recycling is also
79 localised to that region (Engstler et al., 2004; Field and Carrington, 2009; Grünfelder et al.,
80 2003; Link et al., 2021).

81 It was recently shown that the endosomal system of *T. brucei* has a remarkably complex
82 architecture (Link et al., 2023). Rather than being divided into separate compartments, the
83 system forms an interconnected membrane network. Within this network, distinct endosomal
84 functions are grouped into membrane subdomains that are enriched with well-known markers
85 associated with early (TbRab5A), late (TbRab7), and recycling endosomes (TbRab11). While
86 this structure might explain the efficient membrane recycling seen in trypanosomes, the
87 mechanisms responsible for maintaining its stability are not yet understood. One candidate for
88 stabilising and organising this membrane network is the actomyosin system.

89 The actomyosin system of *T. brucei* is very reduced, consisting of one actin gene and two
90 myosin genes (Garcia-Salcedo et al., 2004; Spitznagel et al., 2010). This stands in contrast to
91 its elaborate and highly-structured subpellicular microtubule cytoskeleton (Robinson et al.,
92 1995). Although the exact functions of the reduced actomyosin system in *T. brucei* are not
93 understood, the retention of a minimal system (along with regulatory proteins) suggests an
94 essential function that the microtubule cytoskeleton cannot recapitulate. Previous work on *T.*
95 *brucei* actin showed that its depletion in BSFs resulted in a rapid cell division arrest, loss of
96 endocytic activity, and ultimately cell death (Garcia-Salcedo et al., 2004). Interestingly, *T.*
97 *brucei* filamentous actin has not been visualised by phalloidin binding. This suggests that
98 filamentous actin in trypanosomes may be short and dynamic, as is the case in *Plasmodium*
99 (Schmitz et al., 2005; Schüler et al., 2005), and was recently shown in the related
100 trypanosomatid parasite *Leishmania* (Kotila et al., 2022).

101 To date, the only experimental characterisation of trypanosome myosins was reported by
102 Spitznagel and coworkers in 2010 (Spitznagel et al., 2010). That study focused on
103 Tb927.4.3380 (TbMyo1), which belongs to the ubiquitous class I myosin family. Class I
104 myosins are smaller than conventional (class II) myosins, and do not self-associate into dimers
105 or bipolar filaments. The functions of class I myosins vary from the regulation of membrane
106 tension to participation in endo- and exocytosis, intracellular trafficking, and cell migration
107 (reviewed in Diaz-Valencia et al., 2022). The myosin domain structure usually consists of a
108 conserved motor domain with ATP- and actin-binding regions, a variable number of IQ
109 (calmodulin-binding) motifs which activate the protein in a Ca^{2+} dependent manner, and a
110 cargo-binding tail domain (Masters et al., 2017; Trivedi et al., 2020).

111 In BSF *T. brucei* cells, TbMyo1 partially colocalised with endocytic cargo, late endosomes, and
112 the lysosome (Spitznagel et al., 2010). In addition, the depletion of TbMyo1 resulted in the
113 inhibition of cargo uptake and an enlargement of the flagellar pocket (Spitznagel et al., 2010).
114 These findings supported a proposed function in endocytic trafficking. Although a direct
115 colocalisation of actin and TbMyo1 was not demonstrated, the depletion or drug-induced
116 disruption of actin resulted in a decreased and more diffuse TbMyo1 signal. It remains unclear
117 however, what kind of motor activity TbMyo1 has and whether it functions primarily as a tether
118 or a transporter.

119 The other *T. brucei* myosin (Tb927.11.16310; TbMyo21, sometimes also referred to as Myo13)
120 is part of the kinetoplastida-specific class XXI family (Foth et al., 2006). In *Leishmania*,
121 knockdown of the class XXI myosin was reported to be lethal, with defects in flagellar assembly
122 and a loss of intracellular trafficking (Katta et al., 2009; Katta et al., 2010). This critical role for
123 Myo21 in *Leishmania* have led to interest in it as a potential drug target (Trivedi et al., 2020).
124 In contrast, there has been no published work on TbMyo21, making it unclear whether it might
125 also be a target for therapeutic intervention in *T. brucei*.

126 Here, a combination of different imaging techniques as well as biochemical and biophysical
127 approaches were used to characterise both myosins in BSF *T. brucei* and determine their
128 relationship to the endomembrane system and their corresponding marker proteins. As part of
129 this work, an anti-actin chromobody system was established for the first time in
130 trypanosomatids, thereby enabling simultaneous visualisation of actin and myosin. The results
131 suggest that the actomyosin system of *T. brucei* is involved in post-endocytic membrane
132 trafficking events and maintaining the complex membrane morphology of the endosomal
133 system.

134 **Results**

135 **TbMyo1 is distributed across cytosolic, organelle- and cytoskeleton-associated cellular**
136 **fractions.**

137 Characterisation of TbMyo1 and TbMyo21 was initially carried out in parallel. To detect
138 endogenous TbMyo1, two anti-TbMyo1 antibodies were generated against the tail domain
139 (amino acids 729-1168) of the protein. The specificity of these antibodies was validated using
140 two transgenic cell lines (Figure S1 A – F). The two anti-TbMyo1 antibodies were subsequently
141 used as a 2:1 mix.

142 The same characterisation strategy was followed for the class XXI myosin. TbMyo21 was
143 found to have extremely low expression levels in both BSF and procyclic life cycle stages,
144 however. In addition, the protein could not be confidently localised using widefield microscopy
145 and RNAi experiments showed that it appeared to be non-essential for BSF cell growth (Figure
146 S2 A – D, F). Thus, all further experiments were conducted on TbMyo1.

147 To determine what proportion of TbMyo1 was associated with the cytoskeleton, a two-step
148 biochemical fractionation was carried out (Figure 1 A). Cells expressing cytosolic green
149 fluorescent protein (GFP) were sequentially fractionated using the non-ionic detergents
150 digitonin and IGEPAL. Digitonin preferentially solubilises the plasma membrane and leads to
151 the release of the cytosolic fraction (SN1), while IGEPAL solubilises the organelle fraction
152 (SN2). Samples were subsequently analysed by immunoblotting with fraction-specific marker
153 proteins. As expected, the cytosolic GFP (~ 27 kDa) was efficiently extracted by digitonin and
154 partitioned into the SN1 fraction (Figure 1 B, top panel). The endoplasmic reticulum (ER)
155 luminal chaperone BiP (~ 80 kDa) was not extracted by digitonin and mostly partitioned into
156 the P1 fraction, but was subsequently solubilised by IGEPAL and partitioned into the SN2
157 fraction (Figure 1 B, middle panel). The cytoskeleton-associated paraflagellar rod proteins
158 TbPFR1 and TbPFR2 (~ 69 and 72 kDa) were not solubilised by either detergent and partitioned
159 into first the P1 and then subsequently into the P2 fraction (Figure 1 B, bottom panel, magenta).
160 Interestingly, around half of the TbMyo1 (~ 130 kDa) partitioned into the SN1 fraction,
161 indicating that there is a substantial cytosolic pool. The remaining material (P1) predominantly
162 partitioned into the cytoskeleton-associated P2 fraction (Figure 1 B, bottom panel, green).

163 Quantification of multiple independent experiments indicated that 60% of the GFP signal was
164 in the cytosol (Figure 1 C, SN1, arrow). About 70% of the BiP signal was in the organelle-
165 associated fraction (SN2, arrow) and 95 % of TbPFR1,2 were in the cytoskeleton-associated
166 fraction (P2, arrow). 40% of TbMyo1 was found in both the cytosolic (SN1) and the

167 cytoskeleton (P2) fractions. Only 20 % of TbMyo1 was found in the organelle-associated (SN2)
168 fraction.

169

170 **TbMyo1 translocates filamentous actin at 130 nm/s *in vitro***

171 The presence of a large cytosolic fraction of the monomeric TbMyo1 implied that it might be
172 quite dynamic *in vivo*. Each class of myosins has its own kinetic properties, and consequently
173 can function as either an active motor or a more static tether *in vivo*. The kinetic properties of
174 TbMyo1 have not been investigated to date, so it was unclear whether it moved quickly or
175 slowly on actin. To measure the velocity at which TbMyo1 can translocate actin, full-length
176 recombinant TbMyo1 was purified and *in vitro* actin filament gliding assays were performed
177 (Figure 2). Based on sequence analysis, TbMyo1 is predicted to consist of a large motor domain
178 (cyan), a single calmodulin-binding IQ motif (yellow) and a membrane-binding FYVE-domain
179 (magenta) (Figure 2 A). The full-length protein was expressed in insect cells and purified, with
180 most of the TbMyo1 eluting as a single peak with associated calmodulin (Figure 2 B and C).
181 For the *in vitro* gliding assays, the purified TbMyo1 was biotinylated, immobilised via
182 streptavidin onto a glass surface, and incubated with Alexa488-phalloidin-labelled filamentous
183 actin at 2 mM ATP (Figure 2 D). The translocation of the filamentous actin by the immobilised
184 myosins was observed and characterised quantitatively (Figure 2 E, Methods). The actin
185 filaments were found to move smoothly with a mean gliding velocity of 130 nm/s (Video S1,
186 Figure 2 E). This indicated that TbMyo1 can functionally interact with actin, and can translocate
187 it at comparatively high speed.

188

189 **TbMyo1 is associated with the endocytic and not the biosynthetic pathway.**

190 The ability of TbMyo1 to actively translocate actin suggested that it might be functioning as a
191 motor *in vivo*. To narrow down which pathways and cargoes it might be associated with, its
192 localisation was examined using light microscopy. Previous studies indicated that TbMyo1 is
193 located in the posterior region of the cell and overlaps with parts of the endosomal system
194 (Spitznagel et al., 2010). These findings had not been made using high-resolution microscopy,
195 however, and a potential localisation to the biosynthetic membrane trafficking pathway
196 remained unexplored. Therefore, the localisation of TbMyo1 was examined using expansion
197 microscopy.

198 After expansion of wild-type *T. brucei* cells, endogenous TbMyo1 was mainly detected in the
199 posterior region of the cell between the nucleus (N) and the mitochondrial genome (kinetoplast,
200 K) (Figure 3 A). The fluorescence signal appeared as variable numbers of foci and larger
201 clusters. Although a signal was detected in close proximity to the kinetoplast in some cells, the
202 majority of signals were situated midway between the kinetoplast and the nucleus. These
203 observations were consistent with the localisation described using widefield microscopy
204 (Spitznagel et al., 2010).

205 To determine whether the TbMyo1 foci might be associated with biosynthetic pathways,
206 colabelling experiments were carried out using the ER chaperone BiP, the Golgi marker
207 GRASP, and the lysosome marker p67. The fixed, labelled cells were imaged using both
208 widefield and structured illumination microscopy (SIM). No substantial overlap was seen
209 between TbMyo1 and BiP (Figure 3 B, I and II). Accordingly, the correlation between the two
210 proteins in the population was weak ($\rho = 0.35$) (Figure 3 C). Similarly, TbMyo1 and the Golgi
211 marker GRASP displayed no overlap (Figure 3 B, III and IV) and weak correlation ($\rho = 0.30$)
212 (Figure 3 C). TbMyo1 and the lysosome marker p67 were frequently observed in close
213 proximity in the posterior region of the cell but did not overlap, despite the TbMyo1 signal
214 being close to and sometimes surrounding the p67 signal (Figure 3 B, V and VI). The correlation
215 between the two proteins was moderate ($\rho = 0.43$) compared to the ER and Golgi markers and
216 showed a much larger spread of values (Figure 3 C).

217 To determine the distribution of TbMyo1 relative to endocytic cargo, fluorescent BSA and
218 transferrin were used as markers (Figure 3 D, I and II). TbMyo1 had previously been suggested
219 to overlap with the endosomal system, but this work was conducted using non-physiological
220 cargoes (lectins) as markers (Spitznagel et al., 2010). Here, the physiological cargoes BSA and
221 transferrin were used. The BSA signal was mainly found in a single globular cluster in the
222 posterior region of the cell, which seemed to partially overlap with TbMyo1 (Figure 3 D, I).
223 The transferrin signal was more widely distributed and seemed to have a more substantial
224 overlap with TbMyo1 (Figure 3 D, II). Surprisingly, despite the clear visual overlap of cargo
225 marker and TbMyo1 signals, the correlations were very weak ($\rho = 0.17$ and 0.20, respectively)
226 (Figure 3 E). This might be because colocalisation can be measured in different ways, and
227 correlation is not the same as co-occurrence (reviewed in Aaron et al., 2018). Correlation
228 measures whether two distinct signals change in a similar manner within an overlapping area,
229 while co-occurrence measures the extent of the overlapping area between the two signals. The
230 results here suggest that although the TbMyo1 distribution overlaps with that of endocytic
231 cargo, the signals are not strongly correlated. The implications are addressed in the Discussion.

232 In summary, TbMyo1 did not appear to associate with endomembrane organelles along the
233 biosynthetic pathway (ER, Golgi, lysosome), but did overlap with endocytic cargo.

234

235 **Ultrastructural localisation of TbMyo1**

236 The overlap between TbMyo1 and endocytic cargo strongly suggested that TbMyo1 is
237 associated with the endosomal system, but there are other organelles present in the posterior
238 region of trypanosomes. To test whether endogenous TbMyo1 is indeed primarily associated
239 with the endosomal system, its ultrastructural localisation was investigated using cryo-
240 sectioning and immuno-electron microscopy.

241 The morphology of the immuno-labelled structures was variable and included both vesicles and
242 cisternae with circular or elongated shapes (Figure 4 A – D). The vesicles were found in
243 different sizes ranging from 30 to 100 nm, while the elongated membrane structures were
244 between 20 and 30 nm thick and up to 1 µm long. Interestingly, glycosomes (readily identifiable
245 because of their electron-dense lumen) were also regularly labelled with the anti-TbMyo1
246 antibodies (Figure 4 E).

247 To test whether the membrane structures represented endosomes, the cells were pulsed with
248 BSA conjugated to 5 nm gold as a marker for endocytic uptake (Figure 4 F – H). The 5 nm gold
249 particles were observed inside the membrane structures, confirming their endosomal identity
250 (Figure 4 F – H). In addition, gold particles were found inside coated vesicles and abundantly
251 in the lysosome (Figure 4 H).

252 The total number of gold particles associated with the different subcellular structures was
253 quantified. While the majority of TbMyo1 gold signals were found in the cytoplasm (57%),
254 equal proportions (15%) were found at glycosomes and endosomes, with smaller amounts at
255 the flagellar pocket (8%) and on vesicles (5%) (Figure 4 I). The large proportion of cytoplasmic
256 TbMyo1 was consistent with the large cytosolic fraction previously observed in the biochemical
257 fractionation assays (Figure 1).

258 To determine whether TbMyo1 was associated with a specific subdomain of the endosomal
259 system, further colocalisation experiments were conducted using mNG-TbMyo1 tagged cells
260 and antibodies against TbRab5A, 7, and 11 (Figure S3) (Link et al., 2023). TbRab5A, 7, and
261 11 are markers of early, late, and recycling endosomal subdomains, respectively (Hall et al.,
262 2004; Hall et al., 2005; Silverman et al., 2011; Umaer et al., 2018). TbRab5A and TbRab7 both
263 partially overlapped with TbMyo1 (Figure S3 A). The corresponding correlation coefficients

264 exhibited large variation, underscoring the dynamic nature of both Rabs and TbMyo1 (Figure
265 S3 B). Immunogold labelling assays further demonstrated colocalisation between TbRab5A
266 and TbRab7 with TbMyo1, highlighting that the proteins are found on the same membranous
267 structures (Figure S3 C). In contrast, the calculated correlation coefficient of 0.1 for the
268 combination of TbMyo1 and TbRab11 reflected that these signals barely overlapped (Figure
269 S3 A and B).

270 In summary, ultrastructural analysis of TbMyo1 confirmed its association with early and late
271 endosomal subdomains but not with the exocytic arms of the recycling compartment; TbMyo1
272 was additionally localised it to glycosomes.

273

274 **TbMyo1 is clustered adjacent to the lysosome.**

275 While the immunofluorescence data indicated no consistent overlap between TbMyo1 and the
276 lysosome (Figure 3 B and C), the immuno-electron microscopy data repeatedly showed
277 TbMyo1 close to lysosomal membranes (Figure 4 H and S3 C). To further explore this finding,
278 correlative light and electron microscopy (CLEM) assays were used (Figure 5), as fluorophore-
279 conjugated secondary antibodies can better penetrate cryosections than gold-conjugated ones
280 (van der Beek et al., 2022).

281 To label the endosomes and lysosome, the cells were incubated with dual-labelled Alexa555-
282 BSA-gold prior to fixation and sample embedding. Anti-VSG antibodies (yellow) were used
283 for cell surface labelling and DAPI (grey) to stain DNA, with both signals serving as fiducials
284 for the correlation (Figure 5, panels I – III). As the BSA-gold was additionally conjugated to a
285 fluorophore (Alexa555), its accumulation at the lysosome was first visualised using widefield
286 microscopy (Figure 5 A and B, cyan). The TbMyo1 signal (magenta) was frequently clustered
287 on one side of the lysosomal signal but did not overlap with it. In addition, the TbMyo1
288 fluorescence was found to decorate endosomal membranes filled with gold particles, consistent
289 with the earlier experiments (Figure 5 B, arrow). Finally, TbMyo1 was again observed on
290 glycosomes (Figure 5 C and D, asterisks).

291 In summary, the use of CLEM on cryosections confirmed that TbMyo1 is clustered adjacent to
292 the lysosome and is associated with endosomal membranes and glycosomes. This represents
293 the first use of CLEM on cryosections in trypanosomes, confirming it as a viable experimental
294 approach for *T. brucei*.

295

296 **Visualisation of TbMyo1 and actin overlap using an anti-actin chromobody**

297 In previous studies, *T. brucei* actin was shown to localise to the endosomal system, and TbMyo1
298 localisation was shown to be dependent on actin (Garcia-Salcedo et al., 2004; Spitznagel et al.,
299 2010). Simultaneous imaging of the two proteins in *T. brucei* was not shown however, and
300 consequently, the extent of colocalisation remained unknown. Given that fractionation data had
301 indicated only 40 % of TbMyo1 was cytoskeleton-associated, it seemed likely that the overlap
302 between the two was not total.

303 Actin was previously visualised in *T. brucei* using an anti-actin polyclonal antibody (Garcia-
304 Salcedo et al., 2004). As an alternative approach, an anti-actin chromobody was tested here.
305 Chromobodies are nanobodies (single-domain antibodies) conjugated to a fluorescent protein
306 and can be expressed intracellularly. The anti-actin chromobody used here was previously used
307 to visualise actin in living *Toxoplasma* cells (Periz et al., 2017). It had not been tested whether
308 it could be used in trypanosomatids, however. If the anti-actin chromobody could be shown to
309 work in trypanosomatids, this would potentially enable the study of dynamic actin localisations
310 in live cells in the future.

311 The anti-actin chromobody was first subcloned into a trypanosome tetracycline-inducible
312 expression vector and a stable cell line was generated. The correct insertion of the gene into the
313 genome was validated using PCR (Figure S4 A). Tight and inducible expression of the anti-
314 actin chromobody at the population level was confirmed by immunoblotting (Figure S4 B). At
315 the single-cell level, a fluorescent chromobody signal was only detectable in the presence of
316 tetracycline and was restricted to the posterior region of cells between the nucleus and
317 kinetoplast (Figure 6 A). This matched the previously reported localisation of actin in
318 trypanosomes (Garcia-Salcedo et al., 2004). Although there was cell-to-cell variation in the
319 expression level of the chromobody, the distribution pattern was consistent (Figure S4 C and
320 Figure 6 B).

321 To confirm that the chromobody signal was genuinely reporting on the distribution of
322 filamentous actin, the cells were treated with latrunculin A (LatA) (Figure 6 C). LatA binds
323 actin monomers and prevents them from polymerising to filamentous actin, ultimately resulting
324 in cell death. Previous work on TbMyo1 had already shown that it became delocalised when
325 cells were treated with LatA (Spitznagel et al., 2010). While low concentrations (0.2 μM) of
326 LatA showed a slight delocalisation of the chromobody signal, high concentrations (2 μM)
327 resulted in a strong delocalisation or even loss of the chromobody signal. This strongly

328 suggested that the chromobody was faithfully reporting on the distribution of filamentous actin
329 in the trypanosome cells.

330 Next, the extent of overlap between TbMyo1 and actin was assessed. The signals strongly
331 overlapped in the posterior part of the cell (Figure 6 D). This was reflected in strong correlation
332 between the signals in the population ($\rho = 0.63$) (Figure 6 E). Importantly, the TbMyo1
333 distribution was the same in uninduced and induced cells, indicating that its localisation was
334 not affected by the expression of the chromobody. Of note, the colocalising area was often up
335 to 1 µm away from the kinetoplast/flagellar pocket region (Figure 6 F) and only a minority of
336 cells showed a signal for either TbMyo1, actin, or both adjacent to the kinetoplast (Figure 6 F,
337 I and II). These observations suggested that the actomyosin system is not constitutively present
338 at the flagellar pocket.

339

340 **Actin maintains the morphology of the endosomal system**

341 Lastly, the role of the actin cytoskeleton in stabilising the endosomal system was tested.
342 Endosomes were labelled using ectopic expression of the marker protein EP1, which has
343 previously been shown to label the entire endosomal system and flagellar pocket of BSF
344 trypanosomes (Engstler and Boshart, 2004; Link et al., 2023). EP1, a cell surface protein found
345 in insect-stage trypanosomes, is mostly excluded from the VSG coat of BSF trypanosomes.

346 To test whether the actomyosin system maintains endosomal morphology, the EP1-GFP-
347 expressing cells were treated with 2 µM latrunculin A (LatA) for varying incubation times
348 (Figure 7).

349 Control cells, harvested and fixed after 0 hours of LatA incubation, mostly (~ 85%) exhibited
350 normal morphology. The EP1-GFP fluorescence in the controls was concentrated in the
351 posterior region of the cell and revealed a variable number of high-intensity signals, surrounded
352 and connected by weaker signals. In contrast, the effects of LatA incubation on the EP1-GFP
353 signal mirrored its effects on the chromobody (Figure 7 A). After 1 hour of LatA incubation,
354 50% of the cells displayed morphological changes, including swelling of the cell body in the
355 posterior part and even complete rounding of the cell (Figure 7 B). After a 2-hour incubation
356 with LatA, only 10% of the cells exhibited a typical morphology. At longer incubation times
357 no cells displaying a normal morphology were observed. These morphological changes were
358 accompanied by a redistribution of the EP1-GFP fluorescence signals. Instead of being confined
359 to the posterior region, the EP1-GFP signals increasingly spread throughout the entire

360 cytoplasm. Examination of the ultrastructure of the endosomal system at early timepoints
361 (≤ 60 min LatA incubation) revealed a complete loss of endosomal integrity, resulting in large
362 membrane vesicles filling the space between the flagellar pocket and the lysosome (Figure 7 C).
363 The preservation of the Golgi complex structure in its entirety, as well as the continuing
364 invagination of clathrin-coated pits and presence of clathrin-coated vesicles at the flagellar
365 pocket, underscored the specificity of this phenotype (Figure 7 C). It is noteworthy that even
366 after 30 to 60 minutes of LatA incubation, which led to the complete disruption of the
367 endosomal system, the parasites remained motile. Moreover, an enlargement of the flagellar
368 pocket was not observed in most cells during this period.

369 To test whether TbMyo1 also contributed to endosomal system morphology, experiments were
370 carried out using the TbMyo1 RNAi cell line. Depletion of TbMyo1 caused a very penetrant
371 phenotype, with most of the cells already rounded-up after 24 h of induction (Figure S5 A).
372 These rounded-up cells are not phenotypically informative, but the cells with a less deranged
373 morphology were still capable of internalising BSA and trafficking it to a lysosome-adjacent
374 compartment (Figure S5 A). Depletion of TbMyo1 was confirmed by immunoblotting (Figure
375 S5 B). Population growth curves matched previously-published results, and indicated that 24 h
376 post-induction was an appropriate starting point for phenotypic investigation (Figure S5 C and
377 Spitznagel et al., 2010). In a preliminary electron microscopy analysis of TbMyo1-depleted
378 cells, enlarged endosomal structures were occasionally seen, consistent with the observations
379 made using LatA-treated cells (Figure S5 D). As in the LatA experiments and consistent with
380 the BSA uptake experiments (Figure S5 A), clathrin-coated vesicles in the cytoplasm and
381 clathrin patches on the flagellar pocket membrane were frequently observed, suggesting that
382 endocytosis was not strongly affected. The data therefore specifically suggest that the complex
383 architecture of the endosomal system in trypanosomes is maintained by the actomyosin
384 cytoskeleton.

385 **Discussion**

386 Despite the considerable research focused on the microtubule cytoskeleton of *T. brucei*, its
387 actomyosin system has received relatively little attention. The polarised distribution of
388 actomyosin system proteins to the posterior part of *T. brucei*, and the recent discovery that the
389 endosomal system of this organism is a three-dimensional network rather than isolated
390 compartments, make the actomyosin system a plausible candidate for maintaining endosomal
391 organisation (Link et al., 2023). In this study, the arrangement of myosins and actin in BSF
392 *T. brucei* was revisited using a combination of imaging and biophysical techniques.

393 Initially, both the class I (TbMyo1) and trypanosomatid-specific class XXI (TbMyo21) proteins
394 were investigated. TbMyo21 exhibited minimal expression in both BSF and procyclic form
395 cells however, and no detrimental growth effects were apparent upon depleting TbMyo21 in
396 BSF cells (Figure S2), consistent with previously-published high-throughput data (Alsford et
397 al., 2011). It remains possible that TbMyo21 might be important only in cell cycle stages that
398 cannot be cultivated *in vitro*, such as epimastigotes. Due to its exceedingly low expression
399 levels and non-essential role in BSF *T. brucei*, TbMyo21 is unlikely to be a viable drug target,
400 in contrast to its homologue in *Leishmania* (Trivedi et al., 2020). Subsequent efforts in this
401 study focused on the characterisation of TbMyo1. Of note, preliminary data indicate
402 downregulation of TbMyo1 expression in the procyclic life cycle stage (Figure S2 E), consistent
403 with earlier proteomic experiments (Tinti and Ferguson, 2022). This finding differs with the
404 previous study, where no change in TbMyo1 expression levels was observed after
405 differentiation (Spitznagel et al., 2010). The discrepancy is most likely due to the stronger signal
406 obtained in the present study with the new anti-TbMyo1 antibodies, although more a more
407 rigorous experiment using a loading control with identical expression levels in the two life cycle
408 stages is still needed. This nonetheless suggests that the actomyosin system is not as critical for
409 the viability of procyclic cells, which have a much lower rate of membrane trafficking than the
410 BSF life cycle stage.

411 The biochemical fractionation data indicated that around half of the TbMyo1 was in the
412 cytosolic fraction, while the remaining portion exhibited a strong association with the
413 cytoskeleton fraction (Figure 1). The substantial cytosolic fraction of TbMyo1 could potentially
414 indicate the molecules adopting an auto-inhibited "foldback" configuration (Yang et al., 2009).
415 This is speculation however, and needs to be tested in future *in vitro* assays. The existence of a
416 large cytosolic fraction at steady state might also suggest that TbMyo1 is very dynamic, with a
417 high turnover on the organelles it is associated with.

418 The *in vitro* motility assays indicated that TbMyo1 can translocate filamentous actin with a
419 mean translocation velocity of 130 nm/s, which is significantly faster than the approximately
420 10–50 nm/s measured for some mammalian class I myosins (Giese et al., 2021; Pyrpassopoulos
421 et al., 2012). This relatively high velocity might indicate that TbMyo1 is participating in
422 intracellular trafficking of BSF *T. brucei* and functioning as an active motor rather than a static
423 tether. It should be stressed, however, that this study has not investigated any of TbMyo1's
424 biochemical or mechanical activities *in vivo*, so this remains a hypothesis for now. The *in vitro*
425 motility assay conditions obviously do not replicate the highly complex and dynamic
426 cytoplasmic environment within a trypanosome cell, and multiple regulatory mechanisms,
427 binding partners, and maybe even membrane interactions (see below) will all come into play.

428 Earlier studies examining the localisation of TbMyo1 primarily concentrated on the endocytic
429 pathway (Spitznagel et al., 2010), with little attention given to its potential association with the
430 biosynthetic route. Nevertheless, neither widefield microscopy nor structured illumination
431 microscopy (SIM) displayed any notable overlap between TbMyo1 and markers of the
432 biosynthetic pathway (Figure 3 B and C). The close juxtaposition of endoplasmic reticulum exit
433 sites (ERES) and the Golgi apparatus in *T. brucei* could provide a rationale for why a motor
434 protein like TbMyo1 might be dispensable for mediating transport between these organelles
435 (Sealey-Cardona et al., 2014). While myosins have often been localised to the Golgi in other
436 systems (Avisar et al., 2008; Buss et al., 1998; Perico et al., 2021), these cell types typically
437 have multiple Golgi apparatuses and a more intricate coordination of secretory pathways.

438 Recently, a potential mechanism was discussed in which secretory material in *T. brucei* might
439 move in bulk from the Golgi to the endosomal system (Link et al., 2023). The secretory material
440 would subsequently travel alongside recycled endocytic cargo from the endosomal system to
441 the flagellar pocket and from there to the surface plasma membrane. In this model, it is the
442 endosomal network that serves as a central sorting hub for both secretory and endocytic cargo.
443 Maintenance of its complex three-dimensional morphology might therefore be critical to
444 efficient function, and this is a process that the TbMyo1 and actin could plausibly contribute to.

445 The actomyosin system has often been associated with membrane manipulation in different
446 organisms (Costa et al., 2020; Eitzen, 2003; Khatibzadeh et al., 2013; Lamichhane et al., 2019).
447 Interestingly, it has recently been shown that in *Drosophila* endosomes can organise F-actin
448 and that endosomal actin can affect subcellular tube growth and integrity (Ríos-Barrera and
449 Leptin, 2022). Thus, it could be that the actomyosin system either generates or helps maintain
450 the architecture of the trypanosome endosomal system. Furthermore, the predicted FYVE

451 domain in the TbMyo1 tail domain is predicted to mediate binding to PI(3)P lipids, which are
452 enriched in endosomal membranes in other organisms (Marat and Haucke, 2016). Preliminary
453 data indicate that this FYVE domain can indeed specifically bind to PI(3)P (C. Veigel and F.
454 Zierhut, unpublished observations). So far, nothing is known about the lipid composition of
455 endosomal membranes in trypanosomes, but the presence of a FYVE domain and the
456 enrichment of TbMyo1 at endosomal membranes suggests PI(3)P lipids in the endosomes of
457 trypanosomes too. If so, the expression of the FYVE domain conjugated to GFP might be a
458 useful tool to visualise PI(3)P-enriched membranes in *T. brucei*. It should be stressed that the
459 present study has not rigorously investigated a direct functional role for TbMyo1 in
460 endomembrane function, and any associations that are drawn based on the data here are
461 necessarily speculative. Further experiments using the TbMyo1 RNAi cell line will be needed
462 to explore this point in more detail.

463 In contrast to the results with the biosynthetic markers, physiological endocytic cargo (BSA,
464 transferrin) visually colocalised with TbMyo1, but the correlations were weak ($\rho = 0.17$ and
465 0.20, respectively) (Figure 3 E). This highlights a potentially important point which is often
466 glossed over in colocalisation analyses - correlation and co-occurrence are different concepts,
467 although both are measures of colocalisation (Aaron et al., 2018). Thus, it is possible for two
468 signals to be strongly correlated even if they do not exhibit much spatial overlap/co-occurrence.
469 Conversely, and as here, two signals can exhibit strong overlap/co-occurrence but low
470 correlation. A possible explanation for the low correlation between TbMyo1 and endocytic
471 cargo might be due to topological differences in the signal origin. While TbMyo1 binds to the
472 endosomal membranes from "outside" (the cytosolic side), the cargo is located in the endosome
473 lumen. Closer examination of some of the data used for these analyses revealed that there are
474 many pixels with a value of 0 for transferrin/BSA and a nonzero value for TbMyo1 and vice-
475 versa. The incidence of zero-versus-nonzero values in the two channels will have lowered the
476 correlation coefficient, and in this sense, the correlation coefficients are giving a hint of what
477 the immuno-electron microscopy later confirmed: that the TbMyo1 and cargo are present in the
478 same locations (i.e. cargo-containing endosomes), but in different proportions (Figure 4).

479 Apart from its endosomal localisation, another intriguing observation stemming from the
480 electron microscopy data was the predominant presence of TbMyo1 signals within the
481 cytoplasm (Figure 4). This agrees with the fractionation results (Figure 1) and reaffirms that
482 TbMyo1 has a substantial cytosolic portion under steady-state conditions. However, it is
483 important to note that the actin filaments of trypanosomes have not yet been observed by
484 electron microscopy. Recently, advanced techniques like cryo-transmission electron

485 microscopy and cryo-electron tomography have been applied to explore and visualise actin in
486 other cell types (reviewed in Jung et al., 2020). It would be intriguing to test these techniques
487 for visualising actin in trypanosomes.

488 Interestingly, there was also a clear glycosomal localisation of TbMyo1, which was further
489 confirmed by CLEM (Figure 5, C and D). TbMyo1 was previously found in a glycosomal
490 proteome obtained by mass spectrometry (Vertommen et al., 2008; Supplementary material,
491 Table S2, proteins only detected in bloodstream forms), providing independent validation of
492 the ultrastructural localisation observed here. Glycosomes are related to peroxisomes, and are
493 used to compartmentalise glycolysis in kinetoplastids (Crowe and Morris, 2021). While a
494 connection to the cytoskeleton has been described as a requirement for peroxisome function,
495 inheritance, and maintenance in plants, yeast, and mammalian cells (Neuhaus et al., 2016),
496 nothing has been reported regarding a connection to the cytoskeleton for glycosomes in
497 trypanosomatids. This link between glycosomes and TbMyo1 was unexpected and merits
498 further investigation.

499 The results from the CLEM experiments underscored the proximity between TbMyo1 and the
500 lysosome (Figure 5 A and B). The consistent localisation of TbMyo1 at or close to the
501 endosomal network and lysosomes, coupled with the fact that neither TbMyo1 nor actin
502 accumulated near the flagellar pocket, suggests that the actomyosin system in trypanosomes
503 primarily functions in post-endocytic trafficking events. This encompasses activities related to
504 trafficking within the endosomal system, movement to and from it, or transport to the lysosome.
505 Transport to the lysosome could conceivably be achieved by TbMyo1 interacting with the class
506 II clathrin-coated vesicles that mediate this traffic. Further support for this interpretation comes
507 from the colocalisation studies using antibodies against the endosomal marker proteins
508 TbRab5A, TbRab7, and TbRab11. TbMyo1 exhibited partial overlap with TbRab5A (early
509 endosomes) and TbRab7 (late endosomes), while no overlap was observed with TbRab11
510 (recycling endosomes). These results support the idea that TbMyo1 is implicated in post-
511 endocytic processes rather than engaging in recycling events.

512 Actin and TbMyo1 were both previously localised to the posterior region of *T. brucei* using
513 polyclonal antibodies in the 2004 García-Salcedo et al. and 2010 Spitznagel et al. studies
514 respectively, and the latter paper also showed that disruption of actin using either RNAi or LatA
515 resulted in a more diffuse TbMyo1 signal. Until now, however, TbMyo1 and actin had not been
516 imaged simultaneously in *T. brucei*. Here, the actin cytoskeleton was visualised using an
517 inducible anti-actin chromobody, which enabled colabelling with TbMyo1 (Figure 6). The

518 ability to observe actin distributions in living trypanosome cells will undoubtedly be invaluable
519 for future studies of its intracellular dynamics, although further optimisation is still required.
520 The overnight inductions used here are undoubtedly excessive, and some cells with abnormal
521 morphology could be observed at low frequency. It will be important in the future to do a
522 timecourse experiment to determine the shortest incubation time required for maximal
523 expression of the chromobody. As TbMyo1 is a motor protein, the strong overlap with actin
524 was expected and suggests that actin is highly decorated with TbMyo1. Nevertheless, the
525 number and intensity of signal spots varied from cell to cell. Coupled with the relatively high
526 velocity measured of TbMyo1 on actin, this suggests that the actomyosin system in *T. brucei* is
527 highly dynamic. The obvious next step would be the acquisition of the dynamics of the different
528 endosomal marker proteins and the cytoskeleton *in vivo*.

529 One particular topic that would be worth revisiting in light of the data collected here is the role
530 of trypanosome actin in endocytosis. It was surprising that no strong or consistent signal was
531 seen for either TbMyo1 or actin at the flagellar pocket, and it might be possible that neither are
532 essential for endocytosis to occur. Recent work in mammalian cells has suggested that actin is
533 recruited to endocytic sites primarily when endocytosis stalls, and a similar mechanism could
534 conceivably be at work here (Jin et al., 2022). Regardless, it seems clear that the primary focus
535 and function of trypanosome actin and TbMyo1 is centred on the endosomal system.

536 After confirming TbMyo1's capability to translocate actin and characterising its localisation
537 and overlap with actin, the final question was whether the actomyosin system played a role in
538 maintaining the intricate and continuous nature of the endosomal network. EP1-GFP-
539 expressing cells have previously served as a reliable tool for endosomal system analysis
540 (Engstler and Boshart, 2004; Link et al., 2023). In this study, the response of these cells to LatA
541 treatment was analysed to test the actomyosin system's contribution to maintaining the integrity
542 of endosomal membranes. As LatA results in the depolymerisation of the filamentous actin that
543 TbMyo1 binds to, the phenotypic effects observed are due to compromised function of both
544 actin and TbMyo1. Prolonged treatment led to an increasing proportion of cells exhibiting
545 anomalous morphologies, including swelling of the endosomal membranes, and eventually
546 culminating in a rounded cellular form. The observation of clathrin-coated vesicles at the
547 flagellar pocket as well as the preserved Golgi ultrastructure in the experiment once again
548 suggest a very precise role for the actomyosin system in *T. brucei*. This role is likely directly
549 involved in maintaining the integrity of the endosomal system in BSF cells.

550

551 **Materials and Methods:**

552 **Cell culture and cell lines**

553 *Trypanosoma brucei* monomorphic BSF parasites (Lister strain 427, antigenic type MITat 1.2,
554 clone 221) were cultured in HMI-9 medium (Hirumi and Hirumi, 1989) supplemented with
555 10 % foetal bovine serum (Sigma-Aldrich, USA), 100 U/ml penicillin and 0.1 mg/ml
556 streptomycin. The single marker (SM) cells (Wirtz et al., 1999) were cultivated in the presence
557 of G418 (2.5 µg/ml). For the fractionation experiments, the GFP^{ESPro}-221^{ES}.121^{tet} cell line was
558 used (Batram et al., 2014). This cell line was cultured in the presence of blasticidin (5 µg/ml).
559 Blasticidin was also used for growing the mNG-tagged TbMyo1 and TbMyo21 cells. The
560 TbMyo1 and TbMyo21 RNAi cells were cultivated in the presence of G418 (2.5 µg/ml) and
561 hygromycin (5 µg/ml). The 13-90 cells (Wirtz et al., 1999) used for immunogold experiments
562 were cultivated using hygromycin (5 µg/ml) and G418 (2.5 µg/ml). The transgenic EP1::GFP
563 cells were based on MITat1.2 expressing wild type cells and cultivated in the presence of
564 hygromycin (5 µg/ml) and G418 (15 µg/ml) (Engstler and Boshart, 2004). The cells were
565 maintained at 37 °C and 5 % CO_2 in cell culture flasks with filter lids (Greiner). The cells were
566 split at regular intervals to keep the population density below $1x10^6$ cells/ml. Population density
567 was monitored using a Z2 Coulter Counter (Beckman Coulter).

568

569 **Generation of transgenic cell lines**

570 **mNG-tagged cells**: The 3xTy1-mNG-3xTy1-tagged TbMyo1 and TbMyo21 cell lines were
571 generated via endogenous replacement using a PCR tagging method in the wildtype strain 427
572 (Dean et al., 2015). For this, the pPOTv6-mNG-blast plasmid was used as the template DNA
573 (Dean et al., 2015). This plasmid contains the sequences of the 3xTy1-mNG-3xTy1-tag and a
574 blasticidin resistance gene. The forward primer contained the last 80 bp of the 3' end of the
575 5'UTR and followed by 20 bp of the sequence just upstream of the blasticidin resistance gene
576 start codon in the SK473 plasmid (from Susanne Kramer, University of Würzburg, based on
577 the pPOTv6-mNG-blast plasmid). The reverse primer contained the first 80 bp of the target
578 gene ORF of the TbMyo1 or TbMyo21 excluding the ATG in reverse complement and the last
579 18 bp of the 2nd 3xTy1-tag also in reverse complement.

580 **RNAi cells**: These cells were generated in the SM parental cell line (Wirtz et al., 1999) using
581 the p2T7_TAblue plasmid (Alibu et al., 2005) as a vector. The RNAi target sequences were
582 selected by entering the target gene ORF into the RNAit online tool (Redmond et al., 2003).
583 The selected primer pairs flanked the base pairs 286 – 750 (TbMyo1) or 2137 – 2603

584 (TbMyo21) and also encoded homology arms for ligation into p2T7_TAblue. The RNAi target
585 fragments were amplified by PCR from synthesised copies of Tb*MYO1* and Tb*MYO21* in a
586 pUC57 plasmid (Eurogentec). The fragments were ligated into Eam1105I-cut p2T7_TAblue
587 using *in vivo* assembly (IVA) (Watson and Garcia-Nafria, 2019). DNA sequencing was used to
588 confirm correct incorporation of the inserts.

589 **Actin chromobody cells**: For the subcloning of the actin chromobody sequence from the pAC-
590 TagRFP plasmid (ChromoTek, Germany) into the pLew100_v5_Hyg plasmid (Wirtz et al.,
591 1999), primers were designed with complementary overhangs for *in vivo* assembly (Watson
592 and Garcia-Nafria, 2019). The forward primer overhang sequence was homologous to bases
593 upstream of the HindIII restriction site in the pLew100 plasmid, and the reverse primer
594 overhang was homologous to bases downstream of the BamHI restriction site in the pLew100
595 plasmid. The second segment of the primers exhibited homology regions with the beginning
596 and end of the actin chromobody sequence, respectively.

597

598 **RNAi growth curves**

599 RNAi cells were seeded at $5x10^3$ cells/ml in a volume of 22 ml and divided into two 10 ml
600 aliquots in separate flasks. Tetracycline was added to a final concentration of 1 µg/ml in one
601 flask to induce RNAi and refreshed every 24 h. The cells were split and reseeded after 48 h of
602 induction. The population density of the control and induced TbMyo21 RNAi cells was
603 measured every 24 h over a time course of 96 h using a Z2 Coulter Counter (Beckman Coulter).

604

605 **Differentiation of BSF cells to PCF cells**

606 $2x10^7$ cells were grown to a high density (> $2x10^6$ cell/ml) and harvested by centrifugation
607 (1,000 x *g*, 10 min, RT). The supernatant was discarded, and the cell pellet was resuspended in
608 5 ml DTM (Vassella and Boshart, 1996). One litre DTM medium contains 6.8 g NaCl, 0.4 g
609 KCl, 0.2 g $CaCl_2$, 0.14 g NaH_2PO_4, 0.2 g $MgSO_4$, 7.94 g HEPES, 2.2 g $NaHCO_3$, 1 ml phenol
610 red (10 mg/ml), 20 ml MEM amino acids solution 50x (ThermoFisher, ref.no. 11130036), 10
611 ml MEM non-essential amino acids solution 100x (ThermoFisher, ref.no. 11140035), 1.63 g L-
612 glutamine, 0.293 g L-glutamic acid hydrochloride, 730 µl glycerol, 10 ml MEM vitamin
613 solution 100x (ThermoFisher, ref.no. 11120037), 14 µl *β*-mercaptoethanol, 114 mg Na-
614 pyruvate, 14 mg hypoxanthine, 28.2 mg bathocuproin, 7.5 mg hemin, 640 mg proline and
615 182 mg cysteine. The medium was prepared using ddH_2O and adjusted to pH 7.5. Afterwards,

616 150 ml heat-inactivated (1 hour, 56 °C) foetal calf serum (Sigma-Aldrich, USA) was added,
617 and the medium was sterilised by filtration. After the addition of cis-aconitate to a final
618 concentration of 6 mM the cells were transferred into cell culture flasks and incubated overnight
619 at 27 °C. Most cells had PCF morphology the next morning and could be cultivated in SDM79
620 media (Brun and Schonenberger, 1979) from that point onwards.

621

622 **Expression and purification of full-length TbMyo1**

623 Full-length TbMyo1 was cloned into the pFastBac1 expression vector, flanked by a N-terminal
624 6xHIS-tag for affinity purification and a C-terminal AviTag to allow biotinylation of the
625 protein. The myosin heavy chain was co-expressed in the presence of human calmodulin using
626 a baculoviral/Sf21 system (Batters et al., 2014). All remaining steps were performed at 4 °C.
627 The pellet of 500 ml Sf21 cells was resuspended in lysis buffer (20 mM HEPES pH 7.4, 300
628 mM NaCl, 2 mM $MgCl_2$, 1 mM DTT, 2 mM ATP, 2 µM calmodulin, and EDTA-free protease
629 inhibitor tablets (Roche)) and lysed by sonication (sonicator probe Bandelin HD 2070, 5 min
630 total, at 50 % maximal power). The cell extract was centrifuged at 20,000 rpm in a JA 25.50
631 (Beckman) rotor for 30 min. The filtered lysate was then incubated for 30 min with 1 ml of
632 equilibrated HIS-Select HF Ni-affinity gel (Sigma) and loaded onto a gravity flow column. The
633 resin was washed 5 times with 3 ml of wash buffer (20 mM HEPES, 150 mM NaCl, 1 mM
634 $MgCl_2$, 1 mM DTT, pH 7.4). Subsequently, myosin was eluted with 150 mM imidazole in wash
635 buffer. All elution fractions were pooled, concentrated in a spin concentrator (50k MWOC
636 Amicon) and biotinylated using the BirA enzyme (Gautier and Hinner, 2015). As a final
637 purification step the biotinylated myosin sample was loaded onto a Superdex® 200 10/300
638 column to perform size exclusion chromatography. Peak fractions were analysed using SDS-
639 PAGE, pure fractions were pooled and flash-frozen in liquid nitrogen. The protein was stored
640 at -80 °C.

641

642 **Anti-TbMyo1 antibodies**

643 Anti-TbMyo1 antibodies were generated by immunisation of two rabbits with purified
644 recombinant TbMyo1 (amino acids 729–1,168) (Eurogentec). For recombinant protein
645 expression the TbMyo1 tail was cloned into a pET-28a(+) vector including an N-terminal
646 6xHIS-tag. The protein was expressed in BL21 (DE3) *E. coli* cells for 4 h at 27 °C. Expression
647 was induced with 1 mM of IPTG. Cells were harvested by centrifugation and dissolved in 30
648 ml of lysis buffer (50 mM Tris-HCl pH 7.5, 500 mM NaCl, 40 mM imidazole, 1 mM DTT) and

649 lysed by sonication (sonicator probe Bandeline HD 2070) for 5 min at 50% maximal power.
650 The lysate was centrifuged at 20,000 rpm for 20 min at 4 °C in a JA 25.50 rotor (Beckman) and
651 the supernatant was filtered through a 0.45 µm syringe filter. Subsequently, the supernatant was
652 loaded onto an equilibrated 5 ml HisTrapFF column (GE healthcare) using an ÄKTA pure.
653 After washing the column with lysis buffer, proteins were eluted using 200 mM imidazole in
654 lysis buffer. Pure samples were pooled and concentrated using a spin concentrator (10K MWOC
655 Amicon). As a final step, size exclusion chromatography was conducted. The protein sample
656 was applied to a Superdex® 200 10/300 GL column which was equilibrated in PBS, pure elution
657 fractions were pooled, flash frozen in liquid nitrogen, and stored at -80°C. After validation of
658 specificity, the antisera were mixed in a 2:1 ratio and used as a cocktail in further experiments.

659

660 **Previously published and commercial antibodies**

661 The following primary antibodies have been described previously: mouse anti-Ty1 ("BB2")
662 (Bastin et al., 1996), mouse anti-PFR1,2 ("L13D6") (Kohl et al., 1999), rabbit anti-GFP
663 (Pelletier et al., 2002), rabbit anti-TbBiP (Bangs et al., 1993), mouse anti-p67 (Alexander et al.,
664 2002), rabbit anti-GRASP (He et al., 2004), rat anti-TbRab5A, guinea pig anti-TbRab7 and
665 guinea pig anti-TbRab11(Link et al., 2023)

666 The following antibodies came from commercial sources: goat anti-rabbit (IRDye800CW, LI-
667 COR), goat anti-mouse (IRDye680LT, LI-COR), goat anti-rabbit and anti-mouse antibodies
668 conjugated to AlexaFluor dyes (Molecular Probes).

669

670 **Biochemical fractionation**

671 The cell concentration of the GFP^{ESPro}-221^{ES}.121^{tet} and SM cell lines was measured using a Z2
672 Coulter Counter (Beckman Coulter). The two cell lines were used in a 2:1 ratio to dilute the
673 GFP signal and transferred to 50 ml Falcon tubes and pelleted by centrifugation (1,000 x *g*, 10
674 min, RT). The supernatant was removed, and each cell pellet was resuspended in 500 µl vPBS
675 and pooled into one single microfuge tube. The washed cells were pelleted again by
676 centrifugation (1,000 x *g*, 2 min, RT). A second wash step with 1 ml vPBS was then carried
677 out. After the second wash, the cell pellet was resuspended in 400 µl of 40 µg/ml ultra-pure
678 digitonin (Merck, CAS 11024-24-1) in vPBS and incubated (25 min, RT). A 5 % (20 µl) input
679 (I) sample was then taken. The mixture was then separated by centrifugation (750 x *g*, 5 min,
680 RT) and 320 µl of the cytosolic fraction (SN1) was transferred to a fresh microfuge tube where

681 a 5 % sample was taken. The cell pellet was then resuspended with 1 ml vPBS, and the extracted
682 cells were again pelleted by centrifugation (750 x *g*, 5 min, RT). Afterwards, the extracted cells
683 were resuspended in 400 µl lysis buffer (1 % IGEPAL, 0.1 M PIPES-NaOH pH 6.9, 2 mM
684 EGTA, 1 mM $MgCl_2$, 0.1 mM EDTA, EDTA-free protease inhibitor) and incubated 15 min at
685 RT with 500 rpm agitation. Afterwards, a 5 % sample (P1) was taken, and the lysed cells were
686 pelleted by centrifugation (3,400 x *g*, 2 min, RT). Next, 320 µl of the supernatant (SN2) was
687 transferred to a fresh microfuge tube where a 5 % sample was taken. The cytoskeletal pellet
688 was resuspended in 1 ml vPBS containing EDTA-free protease inhibitors (Roche) and
689 centrifuged again (3,400 x *g*, 2 min, RT). The pellet (P2) was resuspended in 400 µl extraction
690 buffer and a 5% sample was taken. SDS loading buffer was added to the 5% samples (I, SN1,
691 P1, SN2, P2) to a final volume of 40 µl. The samples were boiled at 100 °C for 10 min and
692 stored at – 20 °C prior to use.

693

694 **Immunoblotting**

695 For the preparation of whole cell lysates (WCL), cells were harvested by centrifugation (1,000
696 x *g*, 10 min) and the cell pellet was resuspended in 1 ml vPBS containing EDTA-free protease
697 inhibitor (Roche). The cells were pelleted again by centrifugation (750 x *g*, 3 min, RT) and the
698 supernatant was removed. SDS loading buffer was then added to a final concentration of 2 x
699 10^5 cells/µl. The samples were further denatured by boiling (100 °C, 10 min) and stored at -
700 20 °C until use. SDS-PAGE was carried out using a Mini-PROTEAN® Tetra cell (Bio-Rad),
701 and transfer to nitrocellulose membranes was done using a mini-Trans blot cell (Bio-Rad), both
702 according to the manufacturer's instructions. Protein transfer and equal loading were confirmed
703 using a REVERT total protein stain (LI-COR) according to the manufacturer's instructions.
704 Membranes were blocked using blocking buffer (PBS, 0.3 % (v/v) Tween 20, 10 % (w/v) milk)
705 (30 min, RT, rocker). The membranes were then incubated in primary antibodies diluted in
706 blocking buffer (1 h, RT, roller). After three washes in immunoblot buffer (PBS, 0.3 % Tween
707 20) the membranes were incubated with IRDye-conjugated secondary antibodies diluted in
708 immunoblot buffer (1 h, RT, roller). After another three washes in immunoblot buffer, the
709 membranes were visualised using an Odyssey CLx (LI-COR).

710

711 **Actin filament gliding assay**

712 Motility assay procedures were adapted from those described by (Kron et al., 1991). Clean glass
713 coverslips 24 x 50 mm (VWR) were functionalised with a mixture of mPEG-silane MW 2,000

714 and biotin-PEG-silane MW 3400 (Laysan Bio). In brief, both were dissolved in 80 % ethanol
715 pH 2.0 and mixed in a 20:1 ratio. 100 µl of the PEG-biotin solution was spread on each coverslip
716 and incubated for 30 min at 70 °C. Afterwards the coverslips were washed with ethanol, dried
717 under an air stream, and flow chambers were assembled. C-terminal biotinylated myosin was
718 specifically bound via streptavidin to the functionalised glass surface. Subsequently, the surface
719 of the experimental chamber was blocked with 0.5 mg/ml BSA in assay buffer (25 mM
720 imidazole, 25 mM KCl, 4 mM $MgCl_2$, 1 mM EGTA, pH 7.4) for 3 min. After washing the
721 chamber with assay buffer, Alexa488-phalloidin-labelled rabbit skeletal actin filaments were
722 introduced into the flow cell. The assay was started by adding 2 mM ATP in the assay buffer
723 containing a scavenger system (10 mM DTT, 0.01 mg/ml catalase, 0.05 mg/ml glucose oxidase,
724 1.5 mg/ml glucose) to prevent photobleaching of the fluorescent actin filaments. Actin
725 filaments were recorded by fluorescence imaging using a 488 nm laser (40 mW) and images
726 were taken every 1 s with an EMCCD (Andor iXon3) camera using a Nikon Ti-Eclipse
727 microscope in TIRF mode. Moving filaments were tracked and analysed using the ImageJ
728 plugin MTrackJ and Origin.

729

730 **Preparation of samples for immunofluorescence microscopy**

731 Coverslips were washed in 70 % ethanol and then coated with 0.01 % poly-L-lysine in a 24-
732 well plate (> 20 min, RT) and left to dry. $2x10^6$ cells were taken per coverslip and transferred
733 to 15 ml Falcon tubes. The cells were pelleted by centrifugation (1000 x *g*, 1 min per ml of
734 liquid, RT) in a swing-bucket centrifuge. The supernatant was removed, and the cell pellet was
735 gently resuspended in 1 ml ice-cold vPBS containing EDTA-free protease inhibitor (Roche).
736 The cells were again pelleted by centrifugation (1000 x *g*, 2 min, RT) and subsequently
737 resuspended in 0.5 ml ice-cold vPBS containing EDTA-free protease inhibitor (Roche). 0.5 ml
738 ice-cold 8 % (v/v) paraformaldehyde solution in vPBS containing EDTA-free protease inhibitor
739 (Roche) or ice-cold 8% (v/v) paraformaldehyde solution/ 0.2% (v/v) glutaraldehyde in vPBS
740 containing EDTA-free protease inhibitor (Roche) was added to the resuspended cells.
741 Glutaraldehyde was omitted if a subsequent antibody labelling was performed. The suspension
742 was mixed 1-2 times by inversion and was placed on ice for 10 min. The cells were then moved
743 to RT and were incubated for a further 30 min. Afterwards, the fixed cells were centrifuged at
744 1000 x *g* for 2 min at RT. The supernatant was removed, and the fixed cells were then
745 resuspended in 1 ml RT vPBS containing EDTA-free protease inhibitor (Roche). The cells were
746 attached to the coverslips by centrifugation (1000 x *g*, 1 min, RT); attachment was confirmed

747 visually. If the cells were fixed with 4% (v/v) paraformaldehyde solution and 0.1% (v/v)
748 glutaraldehyde in vPBS containing EDTA-free protease inhibitor (Roche), the coverslips were
749 directly mounted on glass slides after cell attachment. Cells which were fixed with 4%
750 paraformaldehyde solution in vPBS containing EDTA-free protease inhibitor (Roche) were first
751 incubated with 0.25 % (v/v) TritonX-100 in PBS for 5 min at RT to permeabilise the cells. The
752 coverslips were blocked in 1 ml 3 % (w/v) BSA in PBS (30 min, RT), and sequentially
753 incubated with clarified primary and secondary antibodies diluted in PBS (1 h, RT, humidified
754 chamber for each) with three PBS washing steps (3 x 5 min, RT, rocker) after each incubation.
755 After the final wash, glass slides were cleaned with 70 % ethanol and a spot of DAPI-
756 Fluoromount (Southern Biotech) was placed on the surface. The coverslips were rinsed in
757 ddH_2O, carefully dried, and then mounted. For preparation of samples for SIM imaging,
758 different coverslips (high precision, No. 1.5 H) were used. Cells were harvested as above,
759 washed, and fixed in 4 % paraformaldehyde solution (10 min, ice then 30 min, RT). The fixed
760 cells were washed, attached to coverslips, permeabilised (0.25 % Triton X-100 in PBS; 5 min,
761 RT), and then labelled and mounted as described above.

762

763 **Expansion microscopy**

764 Cells were initially prepared in the same way as for immunofluorescence microscopy. After the
765 incubation with secondary antibodies and washing, 1 ml 25 mM MA-NHS (bifunctional cross-
766 linker, prepared immediately prior to use) was added to the coverslips (Truckenbrodt et al.,
767 2019). The coverslips were then incubated on a rocker (30 min, RT). MA-NHS was removed,
768 and the coverslips were washed with 1 ml PBS. To allow cells to equilibrate in the monomer
769 solution (8.625 % (w/v) sodium acrylate, 20 % (w/v) acrylamide, 0.075 % (w/v) bisacrylamide,
770 2 M NaCl in PBS), 1 ml was added and incubated for 5 min at RT. 100 µl of monomer solution,
771 supplemented with 2 µl 10 % (v/v) APS and 2 µl 10 % (v/v) TEMED, was briefly vortexed and
772 a 70 µl drop was placed on a piece of parafilm. Coverslips were transferred with cells facing
773 down onto the drop. The polymerisation was allowed to proceed for 20 minutes at RT in the
774 dark. The resulting gel was peeled off the parafilm and transferred into a 12-well plate, with the
775 coverslip at the bottom. For digestion, 1 ml digestion buffer (0.8 M guanidine HCl, 0.5 % (v/v)
776 Triton X-100, 1 x TAE buffer) was mixed with 10 µl proteinase K (6 U/ ml) and added to gels.
777 Digestion was carried out at 37 °C overnight in the dark. Gels were transferred into 10 cm petri
778 dishes. For expansion, ddH_2O (~ 50 ml) was added until the gels were completely covered. The
779 gels were incubated in the dark at RT for 3 h. The water was changed every hour. To stain

780 nucleic acids, gels were placed in water containing DAPI (Thermo Fisher Scientific, 5 mg/ml)
781 at a 1:1000 dilution and incubated for 30 minutes in the dark. Water was removed as much as
782 possible, and the diameters of the gels were measured with a ruler to estimate expansion. Gels
783 were cut into rectangular pieces using a razor blade (~ 1 cm^2) and transferred into an imaging
784 chamber. A 35 mm glass bottom dish was used as an imaging chamber (Glass Bottom Dish,
785 Thermo Fisher Scientific). The dish was first cleaned with 100 % EtOH. The bottom was
786 covered with 1 ml 0.1 % (v/v) Poly-L-Lysine and incubated for 1 h. Chambers were allowed to
787 air-dry after the lysine was removed.

788

789 **Fluorescence microscopy**

790 Images were acquired using a DMI6000B widefield microscope (Leica Microsystems,
791 Germany) with a HCX PL APO CS objective (100x, NA = 1.4, Leica Microsystems, Germany)
792 and Type F Immersion Oil (refractive index = 1.518, Leica Microsystems, Germany). The
793 microscope was controlled using LAS-X software (Leica). Samples were illuminated with an
794 EL6000 light source (Leica) containing a mercury short-arc reflector lamp (HXP-R120W/45C
795 VIS, OSRAM, Germany). Excitation light was selected by using Y3 (545/25 nm), GFP (470/40
796 nm), and A4 (360/40 nm) bandpass filter cubes (Leica Microsystems, Germany). The power
797 density, measured at the objective focal plane with a thermal sensor head (S175C, Thorlabs),
798 was respectively 0.749 ± 0.086, 0.557 ± 0.069, 0.278 ± 0.076 W/cm2 for the three filters.
799 Emitted light was collected at ranges of 605/70 (Y3), 525/50 nm (GFP), and 470/40 nm (DAPI).
800 The individual exposure times and camera gains were adjusted according to the different
801 samples. The mNG-tagged samples required extremely long exposure times (2 s per z-section).
802 RNAi samples (induced and control) were imaged using identical settings. Differential
803 interference contrast (DIC) was used to visualise cell morphology. 3D recordings of each field
804 of view were obtained using 40 Z-slices (step size = 0.21 µm). Fields of view were selected in
805 the DIC channel in order to blind the user to the fluorescence signal and subjectively select for
806 cells with optimum morphology. Images were captured using a DFC365 FX monochrome CCD
807 camera (Leica, 6.45 µm pixel size). Structured illumination microscopy (SIM) images were
808 acquired using an Elyra S.1 SIM microscope (63x oil objective, NA = 1.4, Zeiss, Germany)
809 controlled by ZEN software (Zeiss, Germany). The microscope was equipped with a sCMOS
810 camera PCO Edge 5.5 (Excelitas PCO GmbH, Germany).

811

812 **Cargo uptake assays**

813 **BSA uptake**: Cells ($2x10^6$ cells per coverslip for widefield microscopy, $1x10^8$ for electron
814 microscopy) were harvested by centrifugation (1000 x *g*, 10 min, 4 ºC) and washed in 1 ml ice-
815 cold Voorheis' modified PBS (vPBS; PBS, 46 mM sucrose, 10 mM glucose). The washed cells
816 were pelleted by centrifugation (750 x *g*, 2 min, 4 ºC), and resuspended in 100 µl ice-cold vPBS.
817 The cells were then incubated at low temperature (10 min, ice) to block endocytosis. During
818 this incubation, the labelled BSA (AlexaFluor555 conjugate, Molecular Probes; Alexa555-
819 BSA-Au, UMC Utrecht) was clarified by centrifugation (750 x *g*, 1 min, RT) and kept on ice
820 in the dark. While for widefield microscopy experiments Alexa555-BSA was added to a final
821 concentration of 600 µg/ml, for electron microscopy experiments Alexa555-BSA-5nm-gold
822 conjugate was added to a final OD = 5. Afterwards, the samples were incubated at low
823 temperature (15 min, on ice, in the dark) to allow the BSA to enter the flagellar pocket. The
824 following temperature shift and additional incubation allowed the endocytosis of BSA (15 min
825 or 30 min, 37 °C, in the dark). To quench the reaction, 1 ml ice-cold vPBS was added. The cells
826 were pelleted by centrifugation (750 x *g*, 2 min, 4 °C) and resuspended in 50 µl vPBS containing
827 EDTA-free protease inhibitor (Roche). The cells were fixed by addition of 0.5 ml ice-cold
828 fixation solution (4% (v/v) paraformaldehyde solution and 0.1% (v/v) glutaraldehyde in vPBS
829 for widefield microscopy, 2% (v/v) paraformaldehyde solution and 0.2% (v/v) glutaraldehyde
830 for electron microscopy) (20 min, on ice, in the dark), followed by a 30 min (widefield
831 microscopy) or 2 h (electron microscopy) incubation at RT (in the dark). Afterwards, the cells
832 were pelleted by centrifugation (750 x *g*, 2 min, RT) and washed in 4 ml vPBS containing
833 EDTA-free protease inhibitor (Roche). The washed cells were again pelleted by centrifugation
834 (750 x *g*, 4 min, RT), resuspended in 1 ml vPBS containing EDTA-free protease inhibitor
835 (Roche) and – for widefield microscopy - attached to the poly-L-lysine-coated coverslips by
836 centrifugation (750 x *g*, 1 min, RT). The coverslips were then mounted on glass slides using
837 DAPI-Fluoromount (Southern Biotech) and imaged immediately. For electron microscopy, the
838 cells were further treated as explained in the sample embedding and immuno-electron
839 microscopy section.

840 **Transferrin uptake**: In general, most preparation steps were performed in the same way as for
841 BSA uptake (see above). After the first washing step, however, the cells were resuspended in 1
842 ml RT vPBS and incubated (15 min, 37 °C) to allow the internalisation of surface-bound
843 transferrin from the cell culture media. Afterwards, the cells were pelleted by centrifugation
844 (1,000 x *g*, 2 min, 4 °C) and resuspended in 50 µl ice-cold vPBS, then incubated at low
845 temperature (10 min, on ice) to block endocytosis. After this incubation time, 0.5 µl of 5 mg/ml
846 transferrin (Tetramethylrhodamine conjugate, ThermoFisher Scientific) was added, mixed by

847 flicking, and incubated (15 min, on ice, in the dark) to allow the transferrin to enter the flagellar
848 pocket. The subsequent temperature shift (30 min, 37 °C, in the dark), fixation, washing step,
849 attachment to the coverslips and mounting onto the glass slides were performed as described in
850 the BSA uptake method (see above). The samples were imaged immediately.

851

852 **Sample embedding for electron microscopy**

853 For Tokuyasu immuno-EM, sample preparation and sectioning were performed as previously
854 described (Link et al., 2023). In brief, $1x10^8$ cells were harvested by centrifugation (1500 x *g*,
855 10 min, 37 °C) and washed with 1 ml trypanosome dilution buffer (TDB; 5 mM KCl, 80 mM
856 NaCl, 1 mM $MgSO_4$, 20 mM Na_2HPO_4, 2 mM NaH_2PO_4, 20 mM glucose). Cells were fixed by
857 adding 4 % (v/v) formaldehyde and 0.4 % (v/v) glutaraldehyde in 0.2 M PHEM buffer (120
858 mM PIPES, 50 mM HEPES, 4 mM $MgCl_2$, 20 mM EGTA, adjusted to pH 6.9 with 1 M NaOH)
859 1:1 to TDB. After 5 min the fixatives were replaced with 2 % (v/v) formaldehyde and 0.2 %
860 (v/v) glutaraldehyde in 0.1 M PHEM for 2 hours at RT. Fixatives were removed by washing
861 and quenched with PBS + 0.15 % (w/v) glycine. Cells were pelleted and resuspended in 200 µl
862 12 % gelatine (Rousselot 250 LP30) in 0.1 M PHEM at 37 °C and pelleted again. The pellets
863 were frozen on ice, cut into smaller blocks, and infused with 2.3 M sucrose overnight at 4 °C.
864 The infused blocks were mounted on metal pins and stored in liquid nitrogen. The gelatine-
865 embedded cells were cryosectioned to 55 nm or 100 nm thick sections at -120 °C or -100 °C,
866 respectively, using a DiATOME diamond knife in a Leica ultracut cryomicrotome (UC7).
867 Sections were picked up and deposited on formvar- and carbon-coated grids using 2.3 M
868 sucrose and 1.8 % (v/v) methylcellulose (MC, Sigma M6385 25 centipoises) mixed 1:1.

869 For high pressure freezing, cells were grown to a density of $1 x10^6$ cells/ml in 50 ml, incubated
870 with LatA for 30 – 60 min and harvested by centrifugation (1000 x g, 10 min, RT). The
871 supernatant was removed to 4 ml, and 4 ml foetal bovine serum was added. The cells were
872 pelleted again (1000 x g, 10 min, RT) and the supernatant was removed to 200 µl. The cells
873 were resuspended in the supernatant, and the suspension was then transferred to a PCR tube
874 and the cells pelleted by centrifugation (1,600 x g, 10 s, RT). The cells were then transferred
875 into a carrier with a closed lid to avoid air inclusions. High pressure freezing (HPF) was started
876 immediately using a Leica EM HPM100. After HPF the samples were transferred to an
877 advanced freeze substitution machine (Leica EM AFS2). Low temperature embedding and
878 polymerisation of Epon raisin (DDSA, MNA, Epon812, 2,4,6
879 Tris(dimethylaminomethyl(phenol))) were then carried out. Ultra-thin cuts (60 nm) were

880 obtained with an ultramicrotome (Leica EM UC7/FC7) and were placed on slotted grids. For
881 contrasting, the slices were incubated in 2 % uranyl acetate for 10 min. Afterwards the grids
882 were washed 3x in ddH_2O (boiled to remove CO2) and incubated for 5 min on 50 % Reynold's
883 lead citrate in a petri dish with NaOH tablets. The grids were again washed 2 x in ddH_2O, dried
884 and stored at RT until imaging.

885

886 **Immuno-electron microscopy**

887 Grids with sections facing down were incubated in a 24-well plate with 2 ml PBS at 37 °C for
888 30 – 60 min to remove gelatine, 2.3 M sucrose and 1.8 % (v/v) MC mixture. Afterwards, the
889 grids were washed on ~ 100 µl drops of PBS + 0.15 % (w/v) glycine and PBS on parafilm at
890 RT (both 3 x 5 min). 100 µl drops represent the standard volume for all non-antibody related
891 steps. Next, blocking was performed in PBS + 0.1 % (v/v) acetylated BSA (BSA-c) + 0.5 %
892 (w/v) cold fish-skin gelatine (FSG) for 30 min. The following primary antibody incubation was
893 done for 1 – 2 hours in PBS + 0.1 % BSA-c + 0.5 % FSG. Afterwards, grids were washed 5 x
894 5 min with PBS + 0.1 % BSA-c + 0.5 % FSG and incubated with corresponding gold or
895 fluorophore-coupled secondary antibodies for 1 – 2 hours. Further washing steps with PBS +
896 0.1 % BSA-c + 0.5 % FSG (3 x 5 min) and PBS (3 x 5 min) followed before all remaining
897 antibodies were fixed with 1.25 % glutaraldehyde for 5 min at RT. After three washing steps
898 with ddH_2O to remove phosphate from the grids, the grids were differently treated if an
899 immunogold or a CLEM assay was performed. For CLEM assays the grids were mounted with
900 ProLong™ Diamond Antifade with DAPI (Life Technologies) between a coverslip and glass
901 slide and imaged using a DMI6000B widefield microscope as described above. Afterwards, the
902 grids were unmounted and washed five times with ddH_2O. Then (for immunogold and CLEM
903 assay), the sample contrast was increased by 5 min incubation on 2 % (v/v) uranyl acetate (UA)
904 in water (pH 7) and 7 min incubation on 1.8 % (v/v) methyl cellulose (MC)/0.3 % (v/v) UA in
905 water (pH 4) (both on ice). Grids were looped out with a metal ring and excess MC/UA was
906 removed with filter paper. Grids were dried for at least 30 min at RT in the metal ring. Grids
907 treated in this way can be stored indefinitely and imaged on an electron microscope when
908 desired.

909

910 **Electron Microscope**

911 A JEOL JEM-1400 Flash scanning transmission electron microscope (STEM) was operated at
912 120 kV with camera system: Matataki Flash 2k x 2k.

913

914 **Flow cytometry**

915 Tetracycline-induced and -uninduced cells ($1x10^6$ per sample) were harvested (1500 x *g*, 3 min,
916 RT), resuspended in 1 ml filtered vPBS, and stored on ice until usage. The fluorescence
917 intensity measurements were carried out with FACSCalibur (BD Bioscience). For the
918 measurement of the fluorescence intensity of the samples the fluorescence channel FL2-H (filter
919 range 564-601 nm) was selected to detect the fluorescence intensity of anti-actin TagRFP signal
920 (detection wavelength 588 nm). The data was visualised using the flow cytometry software BD
921 CellQuest™ Pro.

922

923 **Latrunculin A treatment**

924 Uninduced and induced samples were treated with either 0.2 µM or 2 µM Latrunculin A in
925 DMSO (Sigma, CAS 76343-93-6) up to 4 h at 37 °C. After the Latrunculin treatment, untreated
926 and treated cells were fixed using 4% (v/v) paraformaldehyde solution and 0.1% (v/v)
927 glutaraldehyde in vPBS, attached to coverslips and mounted onto the glass slides as described
928 in the preparation for immunofluorescence microscopy section. The samples were imaged
929 immediately.

930

931

932 **Data analysis**

933 **Image processing:** The microscopy images were processed using FiJi (Schindelin et al., 2012)
934 and a macro was used to generate maximum-intensity projections is a semi-automated
935 workflow (Tim Krüger, University of Würzburg).

936 **Quantification analysis:** The immunoblotting results were qualitatively analysed using Image
937 Studio Lite (LI-COR Biosciences). Background subtraction and signal measurement were
938 carried out using Empiria Studio (LI-COR Biosciences). Normalisation against the Total
939 Protein Stain and quantification were completed using Microsoft Excel. Dot plots were created
940 using the web app PlotsOfData (Postma and Goedhart, 2019).

941 **Correlation analysis:** The correlation analysis was done using FiJi (Schindelin et al., 2012)
942 and a macro for pre-processing the raw data. For this, single cells were selected by using the
943 raw data. Only 1K1N cells were chosen by using the DIC and the blue channel which shows

944 the nucleus and the kinetoplast. The cells were cropped by a square of 130x130 pixels and saved
945 as .tif files. Afterwards, a standardised background noise reduction of the red and green channel
946 using the BioVoxxel 'Convoluted Background Subtraction' plugin was performed. Macros
947 used for opening Bio-Format files were modified from Dr. Jan Brocher/BioVoxxel. Firstly, sum
948 slices projections were prepared and converted to 8-bit images. For the subtraction, the median
949 convolution filter with specific radii was chosen, the radius was selected so that only the signal
950 with the highest intensity was visible. The two channels (green and red) were saved in separate
951 folders. A 2D colocalisation macro was carried out on these images. This macro was adapted
952 from one designed by Zhang & Cordelières (Zhang and Cordelières, 2016). Based on the
953 cytofluorograms generated by this macro, the correlation method was chosen as the Spearman's
954 rank. The Spearman's rank correlation coefficient of each image and marker was copied into
955 an Excel spreadsheet. A dot plot of the results was generated using GraphPad Prism.

956 **CLEM analysis**: The ec-CLEM plug-in in Icy was used for the initial correlation (Paul-
957 Gilloteaux et al., 2017). Adobe Photoshop was used to generate the final overlay of the images.

958

959 **Acknowledgements**

960 Thanks go to the Cell Microscopy Core of UMC Utrecht for their workshop "Cryosectioning
961 and immuno-electron microscopy" and training Fabian Link in the Tokuyasu technique. Katy
962 Schmidt (University of Vienna) provided feedback regarding electron microscopy techniques.
963 Elisabeth Meyer-Natus, Daniela Bunsen, Claudia Gehring-Höhn and Christian Stigloher
964 provided help with the electron microscopy benchwork and assistance with the electron
965 microscope. Nicolas Hagedorn assisted with the flow cytometry experiments. Chris de
966 Graffenried (Brown University) provided protocols and advice on expansion microscopy.
967 Derek Nolan (Trinity College, Dublin) very generously shared unpublished data on TbMyo21
968 and provided feedback and advice. Thanks also go to Tom Beneke, Nicola Jones, and Susanne
969 Kramer for proofreading and providing feedback on the manuscript.

970 Non-commercial antibodies were obtained from the following sources: Cynthia He (National
971 University of Singapore) provided the anti-Ty1 (BB2) antibodies; Keith Gull (University of
972 Oxford) provided the anti-PFR1,2 (L13D6) antibodies, James Bangs (University of Buffalo)
973 provided the anti-p67 and anti-BiP antibodies.

974

975

Funding

Alyssa Borges was supported by the Brazilian agency CAPES (program: CAPES/DAAD—Call No. 22/2018; process 88881.199683/2018-01). Markus Engstler was supported by DFG grants EN305, SPP1726 (Microswimmers—From Single Particle Motion to Collective Behaviour), GIF grant I-473-416.13/2018 (Effect of extracellular *Trypanosoma brucei* vesicles on collective and social parasite motility and development in the tsetse fly) and GRK2157 (3D Tissue Models to Study Microbial Infections by Obligate Human Pathogens), the EU ITN Physics of Motility, and the BMBF NUM Organo-Strat. Markus Engstler is a member of the Wilhelm Conrad Röntgen Center for Complex Material Systems (RCCM). Claudia Veigel was supported by DFG grants SFB 863 (B6), SFB 1032 (B1) and Friedrich Baur Stiftung. The transmission electron microscope was funded by the Deutsche Forschungsgemeinschaft (DFG, German Research Foundation) – 426173797 (INST 93/1003-1 FUGG). This work was funded by remaining money from DFG grant MO 3188/2-1 to Brooke Morriswood.

References

Aaron, J.S., A.B. Taylor, and T.-L. Chew. 2018. Image co-localization – co-occurrence versus correlation. *Journal of Cell Science*. 131.

Alexander, D.L., K.J. Schwartz, A.E. Balber, and J.D. Bangs. 2002. Developmentally regulated trafficking of the lysosomal membrane protein p67 in *Trypanosoma brucei*. *J Cell Sci*. 115:3253-3263.

Alibu, V.P., L. Storm, S. Haile, C. Clayton, and D. Horn. 2005. A doubly inducible system for RNA interference and rapid RNAi plasmid construction in *Trypanosoma brucei*. *Mol Biochem Parasitol*. 139:75-82.

Alsford, S., D.J. Turner, S.O. Obado, A. Sanchez-Flores, L. Glover, M. Berriman, C. Hertz-Fowler, and D. Horn. 2011. High-throughput phenotyping using parallel sequencing of RNA interference targets in the African trypanosome. *Genome Res*. 21:915-924.

Avisar, D., A.I. Prokhnevsky, K.S. Makarova, E.V. Koonin, and V.V. Dolja. 2008. Myosin XI-K Is required for rapid trafficking of Golgi stacks, peroxisomes, and mitochondria in leaf cells of *Nicotiana benthamiana*. *Plant Physiol*. 146:1098-1108.

Bangs, J.D., L. Uyetake, M.J. Brickman, A.E. Balber, and J.C. Boothroyd. 1993. Molecular cloning and cellular localization of a BiP homologue in *Trypanosoma brucei*. Divergent ER retention signals in a lower eukaryote. *J Cell Sci*. 105 (Pt 4):1101-1113.

1008 Bartossek, T., N.G. Jones, C. Schafer, M. Cvitkovic, M. Glogger, H.R. Mott, J. Kuper, M.
1009 Brennich, M. Carrington, A.S. Smith, S. Fenz, C. Kisker, and M. Engstler. 2017.
1010 Structural basis for the shielding function of the dynamic trypanosome variant surface
1011 glycoprotein coat. *Nat Microbiol*. 2:1523-1532.
1012 Bastin, P., Z. Bagherzadeh, K.R. Matthews, and K. Gull. 1996. A novel epitope tag system to
1013 study protein targeting and organelle biogenesis in *Trypanosoma brucei*. *Mol Biochem*
1014 *Parasitol*. 77:235-239.
1015 Batram, C., N.G. Jones, C.J. Janzen, S.M. Markert, and M. Engstler. 2014. Expression site
1016 attenuation mechanistically links antigenic variation and development in *Trypanosoma*
1017 *brucei*. *Elife*. 3:e02324.
1018 Batters, C., H. Ellrich, C. Helbig, K.A. Woodall, C. Hundschell, D. Brack, and C. Veigel. 2014.
1019 Calmodulin regulates dimerization, motility, and lipid binding of Leishmania myosin
1020 XXI. *Proc Natl Acad Sci U S A*. 111:E227-236.
1021 Borges, A.R., F. Link, M. Engstler, and N.G. Jones. 2021. The Glycosylphosphatidylinositol
1022 Anchor: A Linchpin for Cell Surface Versatility of Trypanosomatids. *Front Cell Dev*
1023 *Biol*. 9:720536.
1024 Brun, R., and Schonenberger. 1979. Cultivation and in vitro cloning or procyclic culture forms
1025 of *Trypanosoma brucei* in a semi-defined medium. Short communication. *Acta Trop*.
1026 36:289-292.
1027 Buss, F., J. Kendrick-Jones, C. Lionne, A.E. Knight, G.P. Cote, and J. Paul Luzio. 1998. The
1028 localization of myosin VI at the golgi complex and leading edge of fibroblasts and its
1029 phosphorylation and recruitment into membrane ruffles of A431 cells after growth
1030 factor stimulation. *J Cell Biol*. 143:1535-1545.
1031 Costa, A.R., S.C. Sousa, R. Pinto-Costa, J.C. Mateus, C.D.F. Lopes, A.C. Costa, D. Rosa, D.
1032 Machado, L. Pajuelo, X. Wang, F.-q. Zhou, A.J. Pereira, P. Sampaio, B.Y. Rubinstein,
1033 I. Mendes Pinto, M. Lampe, P. Aguiar, and M.M. Sousa. 2020. The membrane periodic
1034 skeleton is an actomyosin network that regulates axonal diameter and conduction. *eLife*.
1035 9:e55471.
1036 Cross, G.A. 1975. Identification, purification and properties of clone-specific glycoprotein
1037 antigens constituting the surface coat of *Trypanosoma brucei*. *Parasitology*. 71:393-
1038 417.
1039 Crowe, L.P., and M.T. Morris. 2021. Glycosome heterogeneity in kinetoplastids. *Biochem Soc*
1040 *Trans*. 49:29-39.

1041 Dean, S., J. Sunter, R.J. Wheeler, I. Hodkinson, E. Gluenz, and K. Gull. 2015. A toolkit enabling
1042 efficient, scalable and reproducible gene tagging in trypanosomatids. *Open Biol*.
1043 5:140197.
1044 Diaz-Valencia, J.D., L.A. Estrada-Abreo, L. Rodriguez-Cruz, A.R. Salgado-Aguayo, and G.
1045 Patino-Lopez. 2022. Class I Myosins, molecular motors involved in cell migration and
1046 cancer. *Cell Adh Migr*. 16:1-12.
1047 Eitzen, G. 2003. Actin remodeling to facilitate membrane fusion. *Biochim Biophys Acta*.
1048 1641:175-181.
1049 Engstler, M., and M. Boshart. 2004. Cold shock and regulation of surface protein trafficking
1050 convey sensitization to inducers of stage differentiation in *Trypanosoma brucei*. *Genes*
1051 *Dev*. 18:2798-2811.
1052 Engstler, M., T. Pfohl, S. Herminghaus, M. Boshart, G. Wiegertjes, N. Heddergott, and P.
1053 Overath. 2007. Hydrodynamic flow-mediated protein sorting on the cell surface of
1054 trypanosomes. *Cell*. 131:505-515.
1055 Engstler, M., L. Thilo, F. Weise, C.G. Grunfelder, H. Schwarz, M. Boshart, and P. Overath.
1056 2004. Kinetics of endocytosis and recycling of the GPI-anchored variant surface
1057 glycoprotein in *Trypanosoma brucei*. *J Cell Sci*. 117:1105-1115.
1058 Field, M.C., and M. Carrington. 2009. The trypanosome flagellar pocket. *Nat Rev Microbiol*.
1059 7:775-786.
1060 Foth, B.J., M.C. Goedecke, and D. Soldati. 2006. New insights into myosin evolution and
1061 classification. *Proc Natl Acad Sci U S A*. 103:3681-3686.
1062 Garcia-Salcedo, J.A., D. Perez-Morga, P. Gijon, V. Dilbeck, E. Pays, and D.P. Nolan. 2004. A
1063 differential role for actin during the life cycle of *Trypanosoma brucei*. *EMBO J*. 23:780-
1064 789.
1065 Gautier, A., and M.J. Hinner. 2015. Preface. Site-specific protein labeling. *Methods Mol Biol*.
1066 1266:v-viii.
1067 Giese, S., T. Reindl, P.Y.A. Reinke, L. Zattelman, R. Fedorov, A. Henn, M.H. Taft, and D.J.
1068 Manstein. 2021. Mechanochemical properties of human myosin-1C are modulated by
1069 isoform-specific differences in the N-terminal extension. *Journal of Biological*
1070 *Chemistry*. 296:100128.
1071 Grünfelder, C.G., M. Engstler, F. Weise, H. Schwarz, Y.D. Stierhof, M. Boshart, and P.
1072 Overath. 2002. Accumulation of a GPI-anchored protein at the cell surface requires
1073 sorting at multiple intracellular levels. *Traffic*. 3:547-559.

1074 Grünfelder, C.G., M. Engstler, F. Weise, H. Schwarz, Y.D. Stierhof, G.W. Morgan, M.C. Field,
1075 and P. Overath. 2003. Endocytosis of a glycosylphosphatidylinositol-anchored protein
1076 via clathrin-coated vesicles, sorting by default in endosomes, and exocytosis via
1077 RAB11-positive carriers. *Mol Biol Cell*. 14:2029-2040.
1078 Hall, B., C.L. Allen, D. Goulding, and M.C. Field. 2004. Both of the Rab5 subfamily small
1079 GTPases of *Trypanosoma brucei* are essential and required for endocytosis. *Mol*
1080 *Biochem Parasitol*. 138:67-77.
1081 Hall, B.S., E. Smith, W. Langer, L.A. Jacobs, D. Goulding, and M.C. Field. 2005.
1082 Developmental variation in Rab11-dependent trafficking in *Trypanosoma brucei*.
1083 *Eukaryot Cell*. 4:971-980.
1084 Hartel, A.J., M. Glogger, N.G. Jones, W. Abuillan, C. Batram, A. Hermann, S.F. Fenz, M.
1085 Tanaka, and M. Engstler. 2016. N-glycosylation enables high lateral mobility of GPI-
1086 anchored proteins at a molecular crowding threshold. *Nat Commun*. 7:12870.
1087 He, C.Y., H.H. Ho, J. Malsam, C. Chalouni, C.M. West, E. Ullu, D. Toomre, and G. Warren.
1088 2004. Golgi duplication in *Trypanosoma brucei*. *J Cell Biol*. 165:313-321.
1089 Hirumi, H., and K. Hirumi. 1989. Continuous cultivation of *Trypanosoma brucei* blood stream
1090 forms in a medium containing a low concentration of serum protein without feeder cell
1091 layers. *J Parasitol*. 75:985-989.
1092 Jackson, D.G., M.J. Owen, and H.P. Voorheis. 1985. A new method for the rapid purification
1093 of both the membrane-bound and released forms of the variant surface glycoprotein
1094 from *Trypanosoma brucei*. *Biochem J*. 230:195-202.
1095 Jin M, Shirazinejad C, Wang B, Yan A, Schöneberg J, Upadhyayula S, Xu K, Drubin DG. 2022.
1096 Branched actin networks are organized for asymmetric force production during clathrin-
1097 mediated endocytosis in mammalian cells. *Nat Commun.* 13(1):3578.
1098 Jung, M., D. Kim, and J.Y. Mun. 2020. Direct Visualization of Actin Filaments and Actin-
1099 Binding Proteins in Neuronal Cells. *Front Cell Dev Biol*. 8:588556.
1100 Katta, S.S., A.A. Sahasrabuddhe, and C.M. Gupta. 2009. Flagellar localization of a novel
1101 isoform of myosin, myosin XXI, in *Leishmania*. *Mol Biochem Parasitol*. 164:105-110.
1102 Katta, S.S., T.V.S. Tammana, A.A. Sahasrabuddhe, V.K. Bajpai, and C.M. Gupta. 2010.
1103 Trafficking activity of myosin XXI is required in assembly of *Leishmania* flagellum.
1104 *Journal of Cell Science*. 123:2035-2044.
1105 Khatibzadeh, N., A.A. Spector, W.E. Brownell, and B. Anvari. 2013. Effects of plasma
1106 membrane cholesterol level and cytoskeleton F-actin on cell protrusion mechanics.
1107 *PLoS One*. 8:e57147.

1108 Kohl, L., T. Sherwin, and K. Gull. 1999. Assembly of the paraflagellar rod and the flagellum
1109 attachment zone complex during the *Trypanosoma brucei* cell cycle. *J Eukaryot*
1110 *Microbiol*. 46:105-109.
1111 Kotila, T., H. Wioland, M. Selvaraj, K. Kogan, L. Antenucci, A. Jegou, J.T. Huiskonen, G.
1112 Romet-Lemonne, and P. Lappalainen. 2022. Structural basis of rapid actin dynamics in
1113 the evolutionarily divergent *Leishmania* parasite. *Nat Commun*. 13:3442.
1114 Kron, S.J., Y.Y. Toyoshima, T.Q. Uyeda, and J.A. Spudich. 1991. Assays for actin sliding
1115 movement over myosin-coated surfaces. *Methods Enzymol*. 196:399-416.
1116 Lacomble, S., S. Vaughan, C. Gadelha, M.K. Morphew, M.K. Shaw, J.R. McIntosh, and K.
1117 Gull. 2009. Three-dimensional cellular architecture of the flagellar pocket and
1118 associated cytoskeleton in trypanosomes revealed by electron microscope tomography.
1119 *Journal of Cell Science*. 122:1081-1090.
1120 Lamichhane, A.K., H.M. Garraffo, H. Cai, P.J. Walter, K.J. Kwon-Chung, and Y.C. Chang.
1121 2019. A Novel Role of Fungal Type I Myosin in Regulating Membrane Properties and
1122 Its Association with D-Amino Acid Utilization in *Cryptococcus gattii*. *mBio*.
1123 10:e01867-01819.
1124 Link, F., A. Borges, O. Karo, M. Jungblut, T. Müller, E. Meyer-Natus, T. Krüger, S. Sachs,
1125 N.G. Jones, M. Morphew, M. Sauer, C. Stigloher, J.R. McIntosh, and M. Engstler. 2023.
1126 Continuous endosomes form functional subdomains and orchestrate rapid membrane
1127 trafficking in trypanosomes. Cold Spring Harbor Laboratory.
1128 Link, F., A.R. Borges, N.G. Jones, and M. Engstler. 2021. To the Surface and Back: Exo- and
1129 Endocytic Pathways in *Trypanosoma brucei*. *Front Cell Dev Biol*. 9:720521.
1130 Marat, A.L., and V. Haucke. 2016. Phosphatidylinositol 3-phosphates-at the interface between
1131 cell signalling and membrane traffic. *Embo j*. 35:561-579.
1132 Masters, T.A., J. Kendrick-Jones, and F. Buss. 2017. Myosins: Domain Organisation, Motor
1133 Properties, Physiological Roles and Cellular Functions. *Handbook of experimental*
1134 *pharmacology*. 235:77-122.
1135 Mugnier, M.R., C.E. Stebbins, and F.N. Papavasiliou. 2016. Masters of Disguise: Antigenic
1136 Variation and the VSG Coat in *Trypanosoma brucei*. *PLoS Pathog*. 12:e1005784.
1137 Neuhaus, A., C. Eggeling, R. Erdmann, and W. Schliebs. 2016. Why do peroxisomes associate
1138 with the cytoskeleton? *Biochim Biophys Acta*. 1863:1019-1026.
1139 Paul-Gilloteaux, P., X. Heiligenstein, M. Belle, M.C. Domart, B. Larijani, L. Collinson, G.
1140 Raposo, and J. Salamero. 2017. eC-CLEM: flexible multidimensional registration
1141 software for correlative microscopies. *Nat Methods*. 14:102-103.

1142 Pelletier, L., C.A. Stern, M. Pypaert, D. Sheff, H.M. Ngo, N. Roper, C.Y. He, K. Hu, D.
1143 Toomre, I. Coppens, D.S. Roos, K.A. Joiner, and G. Warren. 2002. Golgi biogenesis in
1144 *Toxoplasma gondii*. *Nature*. 418:548-552.
1145 Perico, C., H. Gao, K.J. Heesom, S.W. Botchway, and I.A. Sparkes. 2021. *Arabidopsis thaliana*
1146 myosin XIK is recruited to the Golgi through interaction with a MyoB receptor.
1147 *Commun Biol*. 4:1182.
1148 Periz, J., J. Whitelaw, C. Harding, S. Gras, M.I. Del Rosario Minina, F. Latorre-Barragan, L.
1149 Lemgruber, M.A. Reimer, R. Insall, A. Heaslip, and M. Meissner. 2017. *Toxoplasma*
1150 *gondii* F-actin forms an extensive filamentous network required for material exchange
1151 and parasite maturation. *eLife*. 6:e24119.
1152 Postma, M., and J. Goedhart. 2019. PlotsOfData-A web app for visualizing data together with
1153 their summaries. *PLoS Biol*. 17:e3000202.
1154 Pyrpassopoulos, S., Elizabeth A. Feeser, Jessica N. Mazerik, Matthew J. Tyska, and E.M.
1155 Ostap. 2012. Membrane-Bound Myo1c Powers Asymmetric Motility of Actin
1156 Filaments. *Current Biology*. 22:1688-1692.
1157 Redmond, S., J. Vadivelu, and M.C. Field. 2003. RNAit: an automated web-based tool for the
1158 selection of RNAi targets in *Trypanosoma brucei*. *Mol Biochem Parasitol*. 128:115-
1159 118.
1160 Ríos-Barrera, L.D., and M. Leptin. 2022. An endosome-associated actin network involved in
1161 directed apical plasma membrane growth. *J Cell Biol*. 221.
1162 Robinson, D.R., T. Sherwin, A. Ploubidou, E.H. Byard, and K. Gull. 1995. Microtubule polarity
1163 and dynamics in the control of organelle positioning, segregation, and cytokinesis in the
1164 trypanosome cell cycle. *J Cell Biol*. 128:1163-1172.
1165 Schindelin, J., I. Arganda-Carreras, E. Frise, V. Kaynig, M. Longair, T. Pietzsch, S. Preibisch,
1166 C. Rueden, S. Saalfeld, B. Schmid, J.Y. Tinevez, D.J. White, V. Hartenstein, K. Eliceiri,
1167 P. Tomancak, and A. Cardona. 2012. Fiji: an open-source platform for biological-image
1168 analysis. *Nat Methods*. 9:676-682.
1169 Schmitz, S., M. Grainger, S. Howell, L.J. Calder, M. Gaeb, J.C. Pinder, A.A. Holder, and C.
1170 Veigel. 2005. Malaria parasite actin filaments are very short. *J Mol Biol*. 349:113-125.
1171 Schüler, H., A.K. Mueller, and K. Matuschewski. 2005. Unusual properties of *Plasmodium*
1172 *falciparum* actin: new insights into microfilament dynamics of apicomplexan parasites.
1173 *FEBS Lett*. 579:655-660.

1174 Sealey-Cardona, M., K. Schmidt, L. Demmel, T. Hirschmugl, T. Gesell, G. Dong, and G.
1175 Warren. 2014. Sec16 determines the size and functioning of the Golgi in the protist
1176 parasite, *Trypanosoma brucei*. *Traffic*. 15:613-629.
1177 Silverman, J.S., K.J. Schwartz, S.L. Hajduk, and J.D. Bangs. 2011. Late endosomal Rab7
1178 regulates lysosomal trafficking of endocytic but not biosynthetic cargo in *Trypanosoma*
1179 *brucei*. *Mol Microbiol*. 82:664-678.
1180 Spitznagel, D., J.F. O'Rourke, N. Leddy, O. Hanrahan, and D.P. Nolan. 2010. Identification and
1181 characterization of an unusual class I myosin involved in vesicle traffic in *Trypanosoma*
1182 *brucei*. *PLoS One*. 5:e12282.
1183 Tinti, M., and M.A.J. Ferguson. 2022. Visualisation of proteome-wide ordered protein
1184 abundances in *Trypanosoma brucei*. *Wellcome open research*. 7:34.
1185 Trivedi, D.V., S. Nag, A. Spudich, K.M. Ruppel, and J.A. Spudich. 2020. The Myosin Family
1186 of Mechanoenzymes: From Mechanisms to Therapeutic Approaches. *Annu Rev*
1187 *Biochem*. 89:667-693.
1188 Truckenbrodt, S., C. Sommer, S.O. Rizzoli, and J.G. Danzl. 2019. A practical guide to
1189 optimization in X10 expansion microscopy. *Nat Protoc*. 14:832-863.
1190 Umaer, K., P.J. Bush, and J.D. Bangs. 2018. Rab11 mediates selective recycling and endocytic
1191 trafficking in *Trypanosoma brucei*. *Traffic*. 19:406-420.
1192 van der Beek, J., C. de Heus, N. Liv, and J. Klumperman. 2022. Quantitative correlative
1193 microscopy reveals the ultrastructural distribution of endogenous endosomal proteins. *J*
1194 *Cell Biol*. 221.
1195 Vassella, E., and M. Boshart. 1996. High molecular mass agarose matrix supports growth of
1196 bloodstream forms of pleomorphic *Trypanosoma brucei* strains in axenic culture. *Mol*
1197 *Biochem Parasitol*. 82:91-105.
1198 Vertommen, D., J. Van Roy, J.P. Szikora, M.H. Rider, P.A. Michels, and F.R. Opperdoes. 2008.
1199 Differential expression of glycosomal and mitochondrial proteins in the two major life-
1200 cycle stages of *Trypanosoma brucei*. *Mol Biochem Parasitol*. 158:189-201.
1201 Watson, J.F., and J. Garcia-Nafria. 2019. In vivo DNA assembly using common laboratory
1202 bacteria: A re-emerging tool to simplify molecular cloning. *J Biol Chem*. 294:15271-
1203 15281.
1204 Webster, P., D.C. Russo, and S.J. Black. 1990. The interaction of Trypanosoma brucei with
1205 antibodies to variant surface glycoproteins. *J Cell Sci*. 96 (Pt 2):249-255.

1206 Wirtz, E., S. Leal, C. Ochatt, and G.A. Cross. 1999. A tightly regulated inducible expression
1207 system for conditional gene knock-outs and dominant-negative genetics in
1208 *Trypanosoma brucei*. *Mol Biochem Parasitol*. 99:89-101.
1209 Yang, Y., T.G. Baboolal, V. Siththanandan, M. Chen, M.L. Walker, P.J. Knight, M. Peckham,
1210 and J.R. Sellers. 2009. A FERM domain autoregulates Drosophila myosin 7a activity.
1211 *Proc Natl Acad Sci U S A*. 106:4189-4194.
1212 Zhang, C., and F. Cordelières. 2016. Bioimage Data Analysis. Wiley-VCH.

1213

1214 **Figure legends**

1215 **Figure 1. TbMyo1 has a large cytosolic pool. (A)** Schematic representation of the two-step
1216 fractionation protocol. BSF *T. brucei* cells were mixed with GFP-expressing BSF cells and
1217 extracted with digitonin to release the cytosolic fraction. The permeabilised cells were
1218 subsequently extracted with IGEPAL (non-ionic detergent) to release the organelle fraction.
1219 5% samples of the input (I), supernatant (SN1, SN2) and pellet (P1, P2) fractions were taken at
1220 the indicated points. The samples were separated by SDS-PAGE and analysed by
1221 immunoblotting. **(B)** TbMyo1 is present in both a cytosolic and a cytoskeleton-associated pool.
1222 Exemplary immunoblotting results from the two-step fractionation protocol as described in (A).
1223 Equal fractions (~2%) were loaded in each lane. The cytosolic marker (GFP, ~ 27 kDa) was
1224 mainly detected in the SN1 fraction. The ER chaperone BiP (~ 80 kDa) partitioned into the P1
1225 and then into the SN2 fractions. The flagellar cytoskeleton proteins PFR1,2 (~ 79 + 82 kDa)
1226 partitioned into the P1 and then the P2 fractions. TbMyo1 (~ 130 kDa) was found to be nearly
1227 equally divided between the SN1 and P1 fractions. The P1 fraction almost completely
1228 partitioned into the P2 fraction. Exemplary images from multiple (n = 8) independent
1229 experiments are shown. L, molecular weight ladder. **(C)** Nearly 50% of TbMyo1 is cytosolic.
1230 Quantification of the fractionation immunoblot data (n = 8). The red bars indicate the median.

1231

1232 **Figure 2. TbMyo1 translocates filamentous actin *in vitro*. (A)** Schematic illustration and
1233 structural prediction of the domain architecture of TbMyo1. The motor domain is shown in
1234 cyan, the IQ (calmodulin-binding) motif is shown in yellow, the FYVE domain is shown in
1235 magenta. Regions without domain prediction are displayed in grey. The structural prediction
1236 was generated using AlphaFold (ID: AF-Q585L2-F1). **(B)** Size exclusion profile of affinity-
1237 purified TbMyo1 (Superdex 200 Increase 10/300). The monomeric TbMyo1 fraction eluted in
1238 a single peak at around 12 ml. The 9 ml (void volume) elution peak corresponds to aggregated
1239 protein. **(C)** TbMyo1 eluted mainly in the second protein peak. Samples were taken from the
1240 eluted volumes corresponding to the different protein peaks and analysed by SDS-PAGE.
1241 TbMyo1 (130 kDa) eluted together with human Calmodulin in the 11.5 ml to 12.5 ml elution
1242 fractions. **(D)** Schematic representation of the *in vitro* actin filament gliding assay. Monomeric,
1243 C-terminally biotinylated TbMyo1 was immobilised via streptavidin on a glass surface.
1244 TbMyo1 translocated Alexa488-phalloidin labelled filamentous actin (F-actin) in the presence
1245 of ATP. **(E)** TbMyo1 translocates filamentous actin *in vitro*. Measurements were taken at 22°C
1246 with a final concentration of 2 mM ATP (n = 30 actin filaments). The average velocity was 130
1247 ± 40 nm/s (mean ± SD; Gaussian fit).

1248

1249 **Figure 3. TbMyo1 is associated with the endocytic and not the biosynthetic pathway. (A)**
1250 TbMyo1 is concentrated on structures in the posterior region of the cell. Expansion microscopy
1251 of bloodstream form (BSF) *T. brucei* labelled with anti-tubulin (yellow), anti-TbMyo1
1252 (magenta) and DAPI (cyan). Six exemplary cells are shown (I – VI). For all cells, a magnified
1253 image of the posterior region (boxed area) is shown without the tubulin signal. The TbMyo1
1254 signal was visible as a large cluster of foci in the posterior region between nucleus (N) and
1255 kinetoplast (K). **(B)** TbMyo1 does not colocalise with the ER (BiP, panels I and II), Golgi
1256 apparatus (GRASP, panels III and IV), or lysosome (p67, panels V and VI) markers. Fixed BSF
1257 cells were labelled using the indicated antibodies or tags and imaged using widefield
1258 microscopy and structured illumination microscopy (SIM). Overlay images with DIC and DAPI
1259 are shown for widefield microscopy images; SIM images show a merge of all three fluorescence
1260 channels. Magnified images of the regions of interest for TbMyo1 and the indicated markers
1261 are shown. **(C)** Quantification of correlation between TbMyo1 and organelle marker signals.
1262 Correlation was estimated using Spearman's rank correlation (BiP/TbMyo1 n = 38,
1263 GRASP/TbMyo1 n = 28, p67/TbMyo1 n = 27). The median ρ is represented by a red line and
1264 the corresponding number is written below the data plot. **(D)** TbMyo1 overlaps with endocytic
1265 cargo. Cells expressing mNG-TbMyo1 were incubated with fluorescent cargo, fixed, and
1266 imaged using widefield microscopy. TbMyo1 (green) and the cargo markers (magenta) showed
1267 partial (BSA, panel I) or strong (transferrin, Tf, panel II) overlap. A magnified image of the
1268 fluorescence channels and a merge are shown next to the overlay with DIC. **(E)** Quantification
1269 of correlation between TbMyo1 and endocytic cargo marker signals. Correlation was estimated
1270 using Spearman's rank correlation (BSA/ TbMyo1 n = 69, Tf/ TbMyo1 n = 77). The median
1271 ρ is represented by a red line and the corresponding number is written below the data plot.
1272 Exemplary images from multiple (n > 2) independent experiments are shown.

1273

1274 **Figure 4. Ultrastructural localisation of TbMyo1. (A - H)** TbMyo1 localises to endosomal
1275 tubes, vesicles, glycosomes, the flagellar pocket, and the cytoplasm. Electron micrographs of
1276 cryosections labelled with anti-TbMyo1 and 12 nm gold-conjugated secondary antibodies. For
1277 each panel a raw and a pseudocoloured version of the image are presented. Endosomal tubes
1278 are coloured green. Vesicles are coloured blue. Glycosomes are outlined in yellow. The
1279 lysosome is coloured brown. Gold particles corresponding to TbMyo1 signals are outlined in
1280 magenta. **(F - H)** Cells were incubated with BSA conjugated to 5 nm gold particles prior to
1281 fixation and immunolabelling with anti-TbMyo1. The BSA was observed in vesicles,

1282 endosomes, and the lysosome. **(I)** Distribution of TbMyo1 in the cytoplasm and on subcellular
1283 structures. All gold particles 30 nm or closer to a structure were defined as being on the
1284 structure (based on a conservative calculation that two antibodies, each 15 nm in length, are
1285 between the bound epitope and the gold particle). More than half of the gold particles were
1286 found to be cytoplasmic. The total number of cells and gold particles quantified is indicated.
1287 Abbreviations: axoneme (Ax), flagellum (F), flagellar pocket (FP), plasma membrane (PM),
1288 nucleus (N). Exemplary single- and double-labelled images were chosen from three separate
1289 labelling experiments.

1290

1291 **Figure 5. TbMyo1 is clustered adjacent to the lysosome.** (**A - D)** Correlative light and
1292 electron microscopy (CLEM) imaging of cryosections. To visualise cargo trafficking, cells
1293 were incubated with double-labelled Alexa555- and 5 nm gold-conjugated BSA (cyan) before
1294 fixation. Cryosections were labelled with anti-TbMyo1 (magenta), anti-VSG (yellow), and
1295 DAPI (grey). For each panel an image of the widefield microscopy **(I)**, the electron micrograph
1296 **(II)** and an overlay of both images **(III)** is presented. The electron micrographs are manually-
1297 stitched mosaics composed of multiple (4 – 9) tiled images of higher magnification (15,000x –
1298 25,000x). Note that a fluorescence signal could only be detected at high local concentrations of
1299 Alexa555-BSA-5 nm gold. VSG and DAPI signals were used as fiducials to correlate IF and
1300 EM images. Correlations were made using the ec-CLEM plug-in in Icy for the initial correlation
1301 and Adobe Photoshop for the final overlay. Abbreviations: L – lysosome, * - glycosomes; the
1302 arrow in panel B shows endosomal tubes filled with BSA gold and positive for TbMyo1. Images
1303 show exemplary images from a sample of 17 correlated cells.

1304

1305 **Figure 6. TbMyo1 overlaps extensively but not completely with actin.** (**A)** Imaging of
1306 trypanosome actin using an inducibly-expressed anti-actin chromobody. Tetracycline (Tet) was
1307 used to induce expression of the anti-actin chromobody. Widefield microscopy of fixed cells in
1308 the absence (- Tet) or presence (+ Tet) of tetracycline are shown. The induced (+ Tet) cells
1309 showed a chromobody signal (magenta) in the posterior region of the cell between the nucleus
1310 (N) and kinetoplast (K), consistent with the reported localisation of actin in BSF *T. brucei*.
1311 DNA was stained with DAPI. **(B)** Cell-to-cell variation of the chromobody signal in the
1312 tetracycline-induced population. The intensity but not the distribution of the signal varied from
1313 cell to cell. **(C)** The actin depolymerising drug latrunculin A (LatA) disrupts the chromobody
1314 signal. Widefield microscopy of fixed, induced chromobody cells in the presence of different

1315 LatA concentrations. The cells in the absence of LatA (- LatA) acted as controls. The addition
1316 of 0.2 µM LatA led to a slight blurring of the chromobody signal (magenta), while 2 µM LatA
1317 resulted in strong blurring (**I**) or even loss of signal (**II**) accompanied by a disruption of cell
1318 morphology. **(D)** TbMyo1 strongly overlaps with the anti-actin chromobody signal. Non-
1319 induced cells acted as a control and showed no chromobody signal, with only a TbMyo1 signal
1320 (green). Induced cells displayed both a chromobody (magenta) and a TbMyo1 signal, which
1321 strongly overlapped in the posterior region of the cell. **(E)** Quantification of correlation between
1322 TbMyo1 and actin signals. Correlation was estimated using Spearman's rank correlation (n =
1323 23). The median ρ is represented by a red line and the corresponding number is written above
1324 the data plot. **(F)** Enlarged view of the strong overlap between TbMyo1 and anti-actin
1325 chromobodies in the posterior region of the cell. Magnified images of the posterior region of
1326 four different cells (**I – IV**) are shown. TbMyo1 and the anti-actin chromobodies strongly
1327 overlapped in all cells examined, but the number and intensity of discrete spots varied.

1328

1329 **Figure 7. Actin depolymerisation disrupts the endosomal system.** (A) LatA treatment
1330 perturbs the endosomal system. EP1-GFP expressing cells were incubated with 2 µM LatA for
1331 the indicated time periods, then fixed and imaged using widefield microscopy. DNA was
1332 stained using DAPI. Longer incubation with LatA resulted in aberrant cell morphologies and
1333 an increasingly diffuse EP1-GFP signal. Exemplary cells from a single experiment are shown.
1334 (B) Quantification of the morphological effects of LatA treatment. Cells were manually
1335 classified as displaying normal, swollen posterior, or rounded morphology. The degree of
1336 morphological disruption was proportional to the duration of incubation with LatA. Data
1337 acquired from >200 cells assayed in three independent experiments. **(C)** LatA treatment
1338 disrupts the ultrastructural morphology of the endosomal system. Cells expressing EP1-GFP
1339 were subjected to a 30 – 60 minute incubation with 2 µM LatA, followed by high-pressure
1340 freezing, embedding in Epon, and examination through transmission electron microscopy. The
1341 cytoplasm contained many large and interconnected tubular profiles, consistent with a swollen
1342 endosomal system. An enlargement of the flagellar pocket was additionally observed.
1343 Exemplary cells from a single experiment are shown.

1344

1345 **Supplementary information**

1346 **Figure S1. Generation and validation of TbMyo1 antibodies and cell lines. (A)** Schematic
1347 of the TbMyo1 *in situ* tagging construct integrated into the genome. The construct encoded the

1348 3' end of the Tb*MYO1* 5' UTR, a blasticidin (BlaR) resistance gene, the alpha/beta tubulin
1349 intergenic region (IR), the mNG gene flanked by two 3xTy1 epitope tags, and the 5' end of the
1350 Tb*MYO1* ORF. The sizes of the various elements are shown in the schematic. The 83 bp labels
1351 indicate the homology arms that drive homologous recombination at the *MYO1* locus. The
1352 annealing sites of the two primers used to confirm integration at the endogenous *MYO1* locus
1353 (Bla-F, Myo1-R) are indicated with arrows. Note that the schematic elements are not shown to
1354 scale. **(B)** Correct integration of the TbMyo1 tagging construct at the endogenous locus. The
1355 gDNA of wild-type (427) and 3 candidate mNG-TbMyo1 clones (C1 - C3) was purified and
1356 analysed by PCR. The annealing sites of the PCR primers are shown in panel A above. No
1357 product was observed for the wild-type control. An ~ 1700 bp product was obtained from the
1358 three mNG-TbMyo1 candidates, indicating correct integration. **(C)** Expression of mNG-
1359 TbMyo1. Whole-cell lysates from the three mNG-TbMyo1 clones and a wild-type control were
1360 prepared and analysed by immunoblotting. Anti-TbMyo1(2411) was used as a primary
1361 antibody; anti-TbPFR1,2 (L13D6) antibodies were used to detect the housekeeping proteins
1362 PFR1,2. The endogenous TbMyo1 signal (green) was visible in all lanes at ~130 kDa; C1, C2
1363 and C3 additionally expressed an ~ 170 kDa protein, matching the size of the mNG-TbMyo1.
1364 **(D)** Validation of anti-TbMyo1 specificity. Whole cell lysates from four different cell lines
1365 (wild-type (427), single marker (SM), mNG-TbMyo1 (mNG), TbMyo1 RNAi) were
1366 immunoblotted with two anti-TbMyo1 antisera (2411, 2412). The TbMyo1 RNAi lysates were
1367 obtained from uninduced (-Tet) and tetracycline-induced (+Tet) samples. TbPFR1,2 was used
1368 as a loading control. Both antisera were able to detect the endogenous TbMyo1 protein at ~ 130
1369 kDa. The signal intensities of the 427 cells and the single marker (SM) ones were almost equal,
1370 independent of which antiserum was used. An additional band at ~ 170 kDa was observed in
1371 the mNG-TbMyo1 samples. This upper band could also be detected using anti-Ty1 antibodies
1372 (right-hand image). In the RNAi-induced (+ Tet) cells, the signal from both antisera was
1373 weaker. **(E)** Strong overlap between endogenous and mNG-tagged TbMyo1. The mNG-
1374 TbMyo1 clones were fixed, labelled with anti-TbMyo1 antibodies (magenta), and imaged using
1375 widefield microscopy. DNA (cyan) was stained using DAPI. Both the mNG-TbMyo1 (green)
1376 and the endogenous protein were exclusively localised to the posterior region of the cells.
1377 Identical results were obtained using anti-Ty1 antibodies to label the mNG-TbMyo1. The same
1378 pattern was observed in all three clones; an exemplary image is shown. **(F)** Depletion of
1379 TbMyo1 results in a loss of signal and morphological changes. TbMyo1 RNAi cells were
1380 induced for 48h, fixed, and labelled with anti-TbMyo1 antibodies (magenta). DNA was stained
1381 with DAPI (cyan). Control cells showed an intense signal of TbMyo1 (magenta) between the

1382 nucleus and the kinetoplast. Induced cells showed a nearly complete loss of the signal, with a
1383 small degree of clone-to-clone variation. The morphology of the TbMyo1-depleted cells
1384 changed dramatically, with some cells developing a 'Big Eye' phenotype. The same results
1385 were obtained with three separate clones; an exemplary image is shown.

1386

1387 **Figure S2. TbMyo21 is expressed at an extremely low level. (A)** Generation of mNG-tagged
1388 TbMyo21 cell line. Schematic of the TbMyo21 *in situ* tagging construct integrated into the
1389 genome. The construct encoded the 3' end of the Tb*MYO21* 5' UTR, a blasticidin (BlaR)
1390 resistance gene, the alpha/beta tubulin intergenic region (IR), the mNG gene flanked by two
1391 3xTy1 epitope tags, and the 5' end of the Tb*MYO21* ORF. The sizes of the various elements
1392 are shown in the schematic. The 83 bp labels indicate the homology arms that drive homologous
1393 recombination at the *MYO21* locus. The annealing sites of the primers used to confirm
1394 integration at the endogenous *MYO21* locus (Bla-F, Myo21-R) are indicated with arrows. Note
1395 that the schematic elements are not shown to scale. **(B)** Correct integration of the TbMyo21
1396 tagging construct at the endogenous locus. The gDNA of wild-type (427) and 3 candidate mNG-
1397 TbMyo1 clones (C1 - C3) was purified and analysed by PCR. The annealing sites of the PCR
1398 primers are shown in panel A. No product was observed for the wild-type control (427). An ~
1399 2000 bp product was obtained from the three mNG-TbMyo21 candidates, indicating correct
1400 integration. **(C)** mNG-TbMyo21 is expressed at a very low level relative to TbMyo1. Whole-
1401 cell lysates from a wild-type control, the mNG-TbMyo1 cell line, and the mNG-TbMyo21 cell
1402 line were prepared and analysed by immunoblotting. The endogenous TbMyo1 signal (green)
1403 was visible at ~130 kDa; the mNG-TbMyo1 cell line additionally expressed an ~ 170 kDa
1404 protein, corresponding to mNG-TbMyo1. The anti-Ty1 antibody signal (magenta) required an
1405 overexposure (right hand image) to visualise the mNG-TbMyo21 band at ~ 160 kDa (boxed
1406 area). **(D)** TbMyo21 expression levels are equally low in bloodstream form (BSF) and procyclic
1407 form (PCF) cells. Whole-cell lysates from the mNG-TbMyo21 cell line and a wild-type control
1408 were prepared before and after differentiation to PCF cells and analysed by immunoblotting. A
1409 whole-cell lysate from BSF mNG-TbMyo1 cells served as a positive control. The anti-Ty1
1410 antibody signal (magenta) was only visible in the mNG-TbMyo1 cell line at ~ 170 kDa (left-
1411 hand image). The anti-Ty1 signal required an overexposure to visualise an mNG-TbMyo21
1412 band at ~ 160 kDa (right-hand image). **(E)** TbMyo1 expression is downregulated after
1413 differentiation to PCF cells. The whole-cell lysates from BSF mNG-TbMyo1 cells and both
1414 BSF and PCF wild-type cells were analysed by immunoblotting. Equal numbers of cell
1415 equivalents ($1.4x10^6$) were loaded in each lane. The endogenous TbMyo1 signal (green) was

1416 visible in all lanes at ~130 kDa; the mNG-TbMyo1 cell line additionally expressed an ~ 170
1417 kDa protein, matching the size of the mNG-TbMyo1. Quantification was by direct measurement
1418 of band intensity after background subtraction and without normalisation to a loading control,
1419 and is therefore somewhat tentative. The TbMyo1 signal in PCF cells showed <50% signal
1420 intensity compared to BSF cells. **(F)** TbMyo21 does not appear to be essential for growth *in*
1421 *vitro*. The cell population density of TbMyo21 RNAi cells was measured for 96 hours in
1422 tetracycline uninduced (-Tet) and induced (+Tet) conditions. The cells were diluted after 48
1423 hours to ensure logarithmical growth. Results from three independent experiments using three
1424 separate clones are shown; data points are mean +/- standard deviation.

1425

1426 **Figure S3. TbMyo1 is associated with early and late endosomes. (A)** TbMyo1 signals
1427 partially overlap with TbRab5A and TbRab7 signals, but not with TbRab11 signals.
1428 Colocalisation experiments were conducted using chemically fixed mNG-TbMyo1 cells,
1429 labelled with antibodies against TbRab5A, 7, or 11 and imaged using widefield microscopy.
1430 The fluorescence signals for TbRab5A (I, magenta), TbRab7 (II, magenta), TbRab11 (III,
1431 magenta) and TbMyo1 (I – III, green) were localised between the kinetoplast (K) and the
1432 nucleus (N) of the cells. DNA was stained using DAPI (I – III, cyan). Exemplary cells from
1433 four independent experiments are shown. **(B)** Quantification of correlation between TbMyo1
1434 and TbRab signals. Correlation was estimated using Pearson's correlation coefficient
1435 (TbRab5A/TbMyo1, n = 66; TbRab7/TbMyo1, n = 73; TbRab11/TbMyo1, n = 86). Red bars
1436 indicate the median R; median R values for each pair are shown above the dot plot. **(C)** Electron
1437 micrographs of cryosections colabelled with anti-TbMyo1 and anti-TbRab5A or anti-TbRab7
1438 antibodies. For each panel a raw and a pseudocoloured version of the image are presented.
1439 Endosomal membranes are coloured green. The lysosome is coloured brown. Gold particles
1440 corresponding to TbMyo1 signals are outlined in green. Gold particles corresponding to
1441 TbRab5A or TbRab7 signals are outlined in magenta. Exemplary cells from a single labelling
1442 experiment are shown.

1443

1444 **Figure S4. Generation and validation of the anti-actin chromobody cell line. (A)**
1445 Integration of the anti-actin TagRFP chromobody construct. The gDNA of wild-type (SM) and
1446 3 candidate clones (C1, C2, C4) was purified and analysed by PCR using primers specific for
1447 the chromobody. No product was observed for the wild-type control. An ~ 1200 bp product was
1448 obtained from the three candidates, indicating integration into the genome. **(B)** Tight and

1449 inducible expression of the anti-actin TagRFP chromobody. Whole-cell lysates from the three
1450 clones (tetracycline-induced and -uninduced) and a wild-type control (SM) were prepared and
1451 analysed by immunoblotting, using anti-RFP antibodies. No signal was detected in the control
1452 sample and in the uninduced (-) chromobody clones. In the induced (+) samples, a protein band
1453 at ~40 kDa was detected in all three clones. The expected size of the anti-actin chromobody is
1454 41.5 kDa. **(C)** Varying anti-actin TagRFP chromobody expression levels in the three clones.
1455 The three clones (C1, C2, C4) were analysed 24 hours after induction with tetracycline and RFP
1456 signal was measured using flow cytometry. Wild-type cells (SM) served as a control. All clones
1457 showed a significant increase in fluorescence counts in the RFP channel relative to control cells,
1458 with some clone-to-clone variation in expression levels.

1459

1460 **Figure S5. TbMyo1 depletion affects cell morphology and endosomal membrane**
1461 **organisation. (A)** Bovine serum albumin (BSA) is still internalised after TbMyo1 depletion.
1462 TbMyo1 depletion was induced by RNAi for 0, 24, and 48 hours. The cells were then harvested
1463 and incubated with fluorophore-conjugated BSA (yellow) for 30 minutes at 37°C. The cells
1464 were then fixed with formaldehyde and immunolabeled with anti-p67 antibodies (magenta),
1465 and DNA was stained with DAPI (cyan). Exemplary DIC fields of view are presented alongside
1466 enlarged views of selected morphologically normal cells (I-III). Prolonged protein depletion led
1467 to an increased number of cells displaying a rounded morphology. In cells with normal
1468 morphology, fluorescent BSA strongly overlapped with p67, indicating normal cargo uptake.
1469 Results obtained in a single experiment using three separate TbMyo1 RNAi clones. **(B)**
1470 Confirmation of TbMyo1 depletion. Whole-cell lysates from three different TbMyo1 RNAi
1471 clones were collected at 0, 24, and 48 h and analysed by immunoblotting. The TbMyo1 signal
1472 (green) was observed at ~130 kDa, with signal intensity significantly decreasing at 24 h and 48
1473 h in all three clones. Antibodies against TbPFR1,2 were used as loading controls to check for
1474 equal sample loading. **(C)** TbMyo1 is essential for *in vitro* growth. The cell population density
1475 of TbMyo1 RNAi cells was measured over 96 hours under control (-tet) and induced (+tet)
1476 conditions. Cells were diluted after 48 hours to maintain logarithmic growth. Results from two
1477 independent experiments, each using three separate clones, are shown; data points represent the
1478 mean +/- standard deviation. **(D)** TbMyo1 depletion results in ultrastructural changes in
1479 endosomal membranes. BSF TbMyo1 RNAi cells were incubated for 24 h to induce TbMyo1
1480 depletion, followed by high-pressure freezing, embedding in Epon, and examination via
1481 transmission electron microscopy. Most cells exhibited either a normal ultrastructure (I) or an

1482 extremely enlarged flagellar pocket (V and VI). A subset of cells displayed numerous large and
1483 interconnected tubular profiles, suggestive of a swollen endosomal system. Exemplary cells
1484 from a single experiment are shown. Abbreviations: clathrin-coated pit: CCP, clathrin-coated
1485 vesicle: CCV, endosomal membranes: E, flagellar pocket: FP, Golgi apparatus: G,
1486 mitochondrion: M, nucleus: N.

1487

1488 **Video S1. TbMyo1 translocate filamentous actin *in vitro*.** Rhodamine-phalloidin-stained
1489 actin filaments gliding over a coverslip decorated with full-length TbMyo1 molecules. Buffer
1490 contained 2 mM ATP. Images were acquired at a rate of 1 frame/s. Playback rate 50 frames/s.
1491 Scale bar 5 μm.

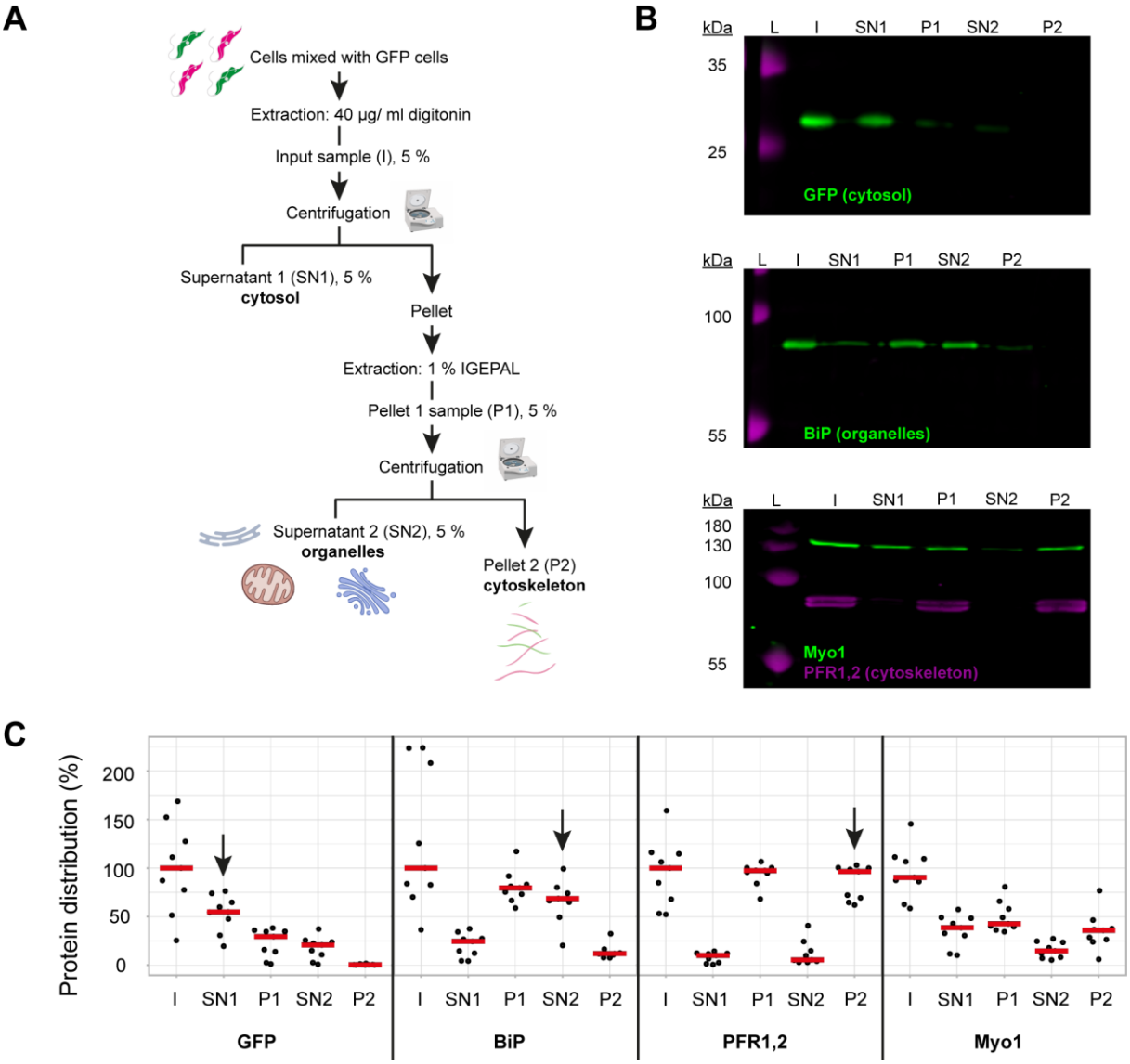

Figure 1. TbMyo1 has a large cytosolic pool. (A) Schematic representation of the two-step fractionation protocol. BSF *T. brucei* cells were mixed with GFP-expressing BSF cells and extracted with digitonin to release the cytosolic fraction. The permeabilised cells were subsequently extracted with IGEPAL (non-ionic detergent) to release the organelle fraction. 5% samples of the input (I), supernatant (SN1, SN2) and pellet (P1, P2) fractions were taken at the indicated points. The samples were separated by SDS-PAGE and analysed by immunoblotting. **(B)** TbMyo1 is present in both a cytosolic and a cytoskeleton-associated pool. Exemplary immunoblotting results from the two-step fractionation protocol as described in (A). Equal fractions (~ 2%) were loaded in each lane. The cytosolic marker (GFP, ~ 27 kDa) was mainly detected in the SN1 fraction. The ER chaperone BiP (~ 80 kDa) partitioned into the P1 and then into the SN2 fractions. The flagellar cytoskeleton proteins PFR1,2 (~ 79 + 82 kDa) partitioned into the P1 and then the P2 fractions. TbMyo1 (~ 130 kDa) was found to be nearly equally divided between the SN1 and P1 fractions. The P1 fraction almost completely partitioned into the P2 fraction. Exemplary images from multiple (n = 8) independent experiments are shown. L, molecular weight ladder. **(C)** Nearly 50% of TbMyo1 is cytosolic. Quantification of the fractionation immunoblot data (n = 8). The red bars indicate the median.

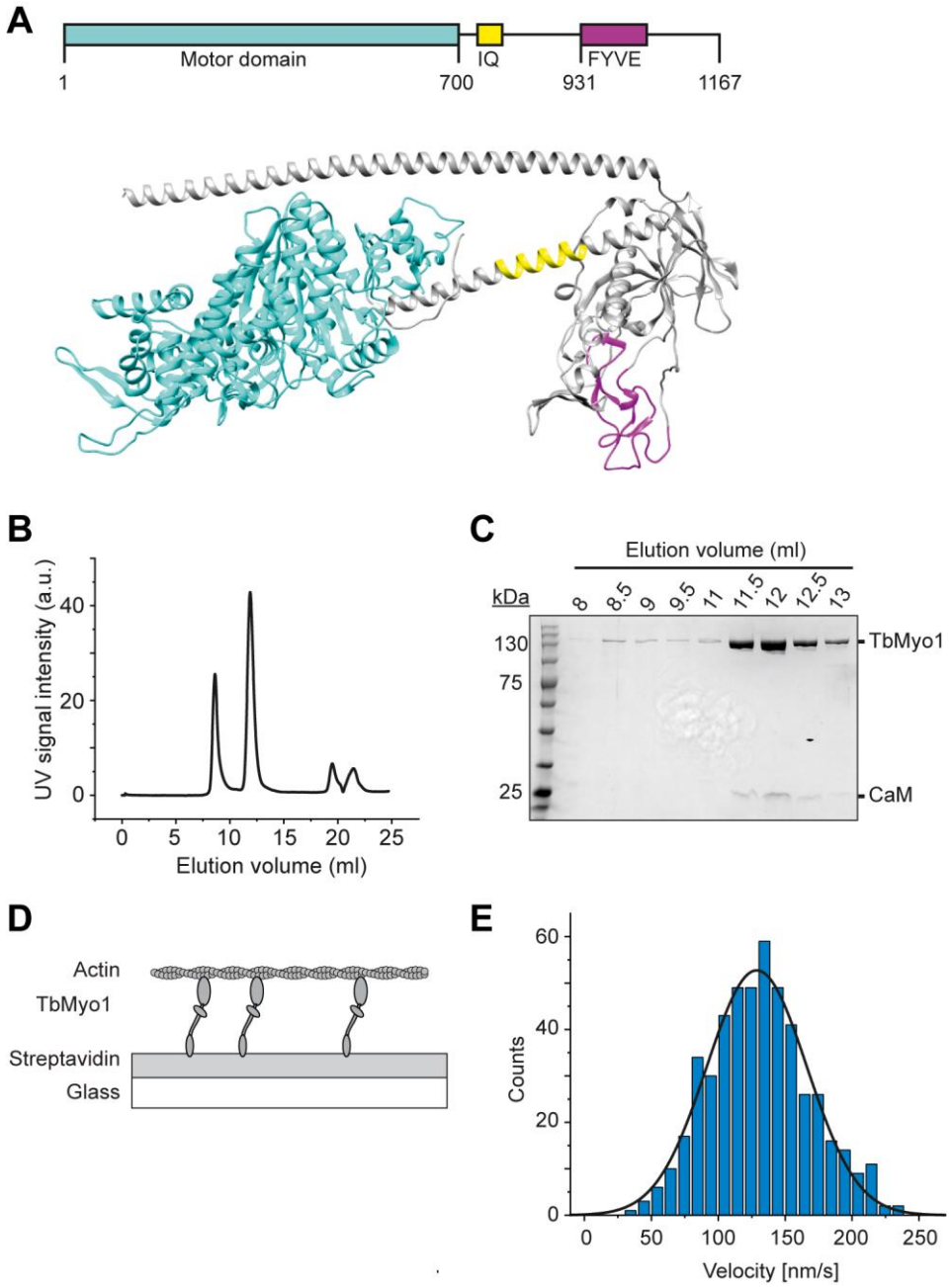

Figure 2. TbMyo1 translocates filamentous actin *in vitro*. (A) Schematic illustration and structural prediction of the domain architecture of TbMyo1. The motor domain is shown in cyan, the IQ (calmodulin-binding) motif is shown in yellow, the FYVE domain is shown in magenta. Regions without domain prediction are displayed in grey. The structural prediction was generated using AlphaFold (ID: AF-Q585L2-F1). **(B)** Size exclusion profile of affinity-purified TbMyo1 (Superdex 200 Increase 10/300). The monomeric TbMyo1 fraction eluted in a single peak at around 12 ml. The 9 ml (void volume) elution peak corresponds to aggregated protein. **(C)** TbMyo1 eluted mainly in the second protein peak. Samples were taken from the eluted volumes corresponding to the different protein peaks and analysed by SDS-PAGE. TbMyo1 (130 kDa) eluted together with human Calmodulin in the 11.5 ml to 12.5 ml elution fractions. **(D)** Schematic representation of the *in vitro* actin filament gliding assay. Monomeric, C-terminally biotinylated TbMyo1 was immobilised via streptavidin on a glass surface. TbMyo1 translocated Alexa488-phalloidin labelled filamentous actin (F-actin) in the presence of ATP. **(E)** TbMyo1 translocates filamentous actin *in vitro*. Measurements were taken at 22°C with a final concentration of 2 mM ATP (n = 30 actin filaments). The average velocity was 130 ± 40 nm/s (mean ± SD; Gaussian fit).

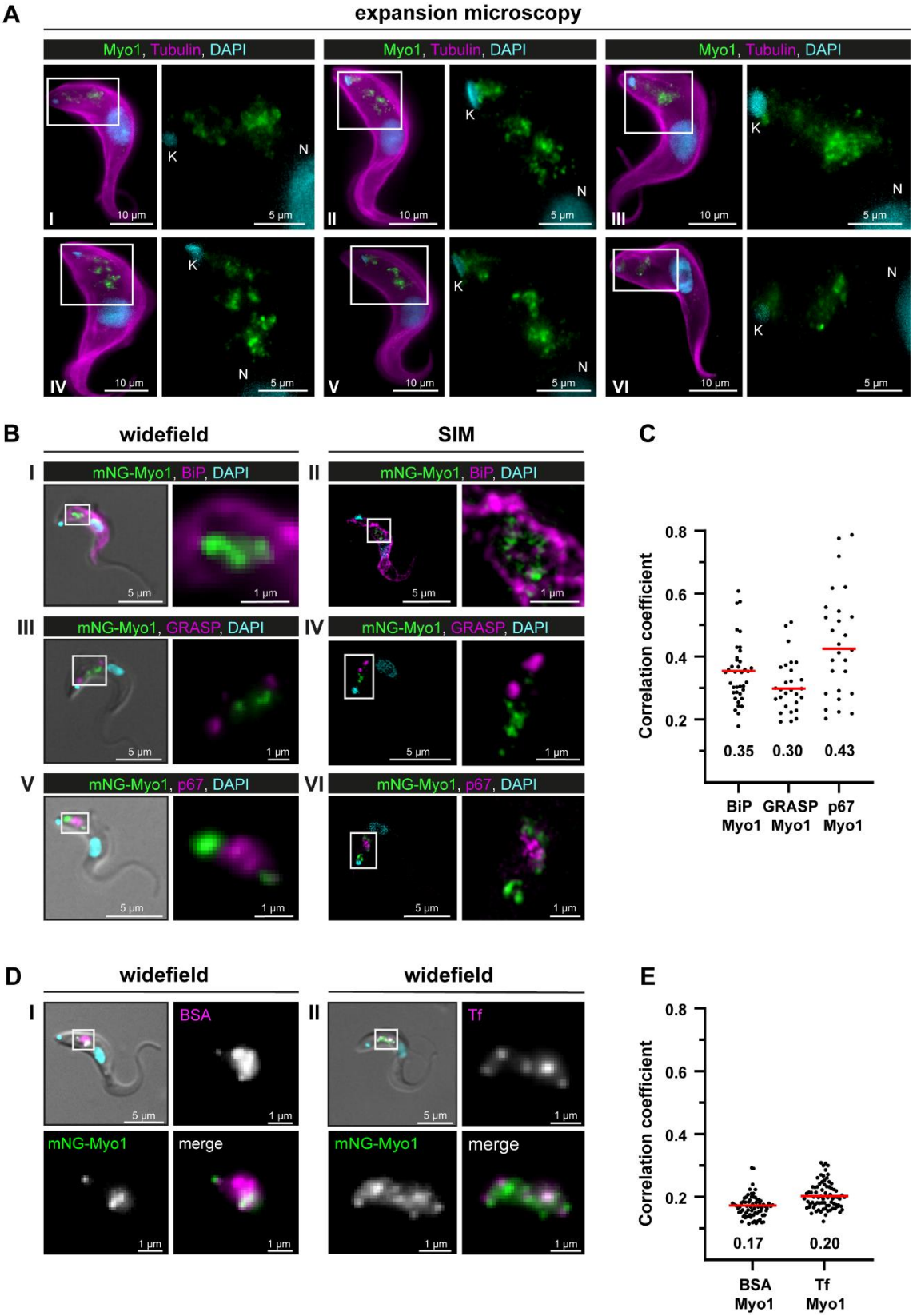
A
expansion microscopy
Myo1, Tubulin, DAPI
K
N
10 µm
5 µm
I
II
III
IV
V
VI
B
widefield
SIM
mNG-Myo1, BiP, DAPI
mNG-Myo1, GRASP, DAPI
mNG-Myo1, p67, DAPI
5 µm
1 µm
C
Correlation coefficient
0.8
0.6
0.4
0.2
0.35
0.30
0.43
BiP Myo1
GRASP Myo1
p67 Myo1
D
widefield
BSA
Tf
mNG-Myo1
merge
E
0.17
0.20
BSA Myo1
Tf Myo1

Figure 3. TbMyo1 is associated with the endocytic and not the biosynthetic pathway. (A) TbMyo1 is concentrated on structures in the posterior region of the cell. Expansion microscopy of bloodstream form (BSF) *T. brucei* labelled with anti-tubulin (yellow), anti-TbMyo1 (magenta) and DAPI (cyan). Six exemplary cells are shown (I – VI). For all cells, a magnified image of the posterior region (boxed area) is shown without the tubulin signal. The TbMyo1 signal was visible as a large cluster of foci in the posterior region between nucleus (N) and kinetoplast (K). **(B)** TbMyo1 does not colocalise with the ER (BiP, panels I and II), Golgi apparatus (GRASP, panels III and IV), or lysosome (p67, panels V and VI) markers. Fixed BSF cells were labelled using the indicated antibodies or tags and imaged using widefield microscopy and structured illumination microscopy (SIM). Overlay images with DIC and DAPI are shown for widefield microscopy images; SIM images show a merge of all three fluorescence channels. Magnified images of the regions of interest for TbMyo1 and the indicated markers are shown. **(C)** Quantification of correlation between TbMyo1 and organelle marker signals. Correlation was estimated using Spearman's rank correlation (BiP/TbMyo1 n = 38, GRASP/TbMyo1 n = 28, p67/TbMyo1 n = 27). The median r is represented by a red line and the corresponding number is written below the data plot. **(D)** TbMyo1 overlaps with endocytic cargo. Cells expressing mNG-TbMyo1 were incubated with fluorescent cargo, fixed, and imaged using widefield microscopy. TbMyo1 (green) and the cargo markers (magenta) showed partial (BSA, panel I) or strong (transferrin, Tf, panel II) overlap. A magnified image of the fluorescence channels and a merge are shown next to the overlay with DIC. **(E)** Quantification of correlation between TbMyo1 and endocytic cargo marker signals. Correlation was estimated using Spearman's rank correlation (BSA/ TbMyo1 n = 69, Tf/ TbMyo1 n = 77). The median r is represented by a red line and the corresponding number is written below the data plot. Exemplary images from multiple (n > 2) independent experiments are shown.

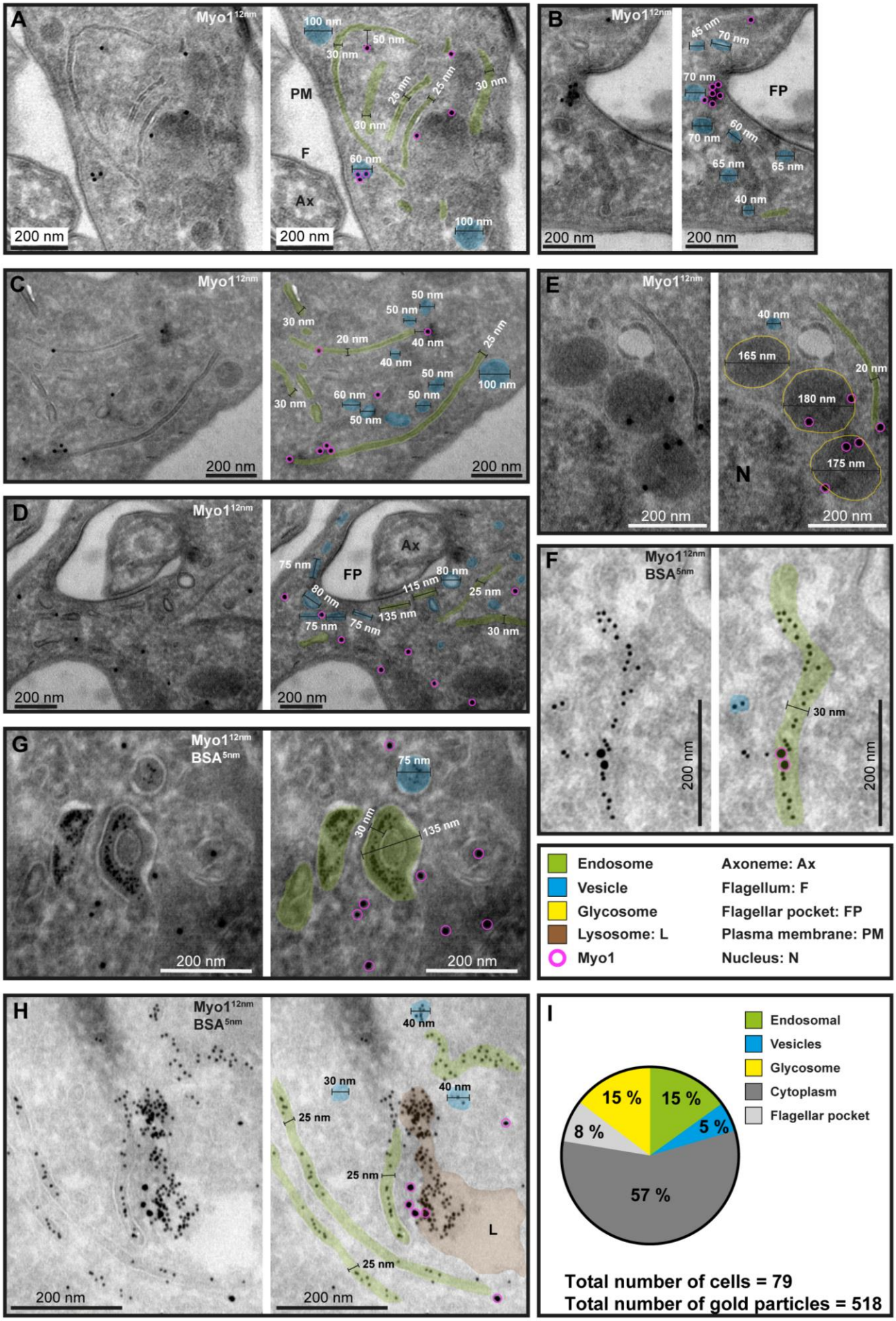
A
Myo1 12nm
PM
F
Ax
100 nm
50 nm
30 nm
25 nm
60 nm
200 nm
B
Myo1 12nm
FP
45 nm
70 nm
60 nm
65 nm
40 nm
C
Myo1 12nm
20 nm
40 nm
50 nm
100 nm
D
Myo1 12nm
Ax
FP
75 nm
80 nm
115 nm
135 nm
E
Myo1 12nm
N
165 nm
180 nm
175 nm
F
Myo1 12nm
BSA 5nm
G
Myo1 12nm
BSA 5nm
H
Myo1 12nm
BSA 5nm
L
Endosome
Vesicle
Glycosome
Lysosome: L
Myo1
Axoneme: Ax
Flagellum: F
Flagellar pocket: FP
Plasma membrane: PM
Nucleus: N
I
Endosomal
Vesicles
Glycosome
Cytoplasm
Flagellar pocket
15 %
15 %
5 %
8 %
57 %
Total number of cells = 79
Total number of gold particles = 518

Figure 4. Ultrastructural localisation of TbMyo1. (A - H) TbMyo1 localises to endosomal tubes, vesicles, glycosomes, the flagellar pocket, and the cytoplasm. Electron micrographs of cryosections labelled with anti-TbMyo1 and 12 nm gold-conjugated secondary antibodies. For each panel a raw and a pseudocoloured version of the image are presented. Endosomal tubes are coloured green. Vesicles are coloured blue. Glycosomes are outlined in yellow. The lysosome is coloured brown. Gold particles corresponding to TbMyo1 signals are outlined in magenta. **(F - H)** Cells were incubated with BSA conjugated to 5 nm gold particles prior to fixation and immunolabelling with anti-TbMyo1. The BSA was observed in vesicles, endosomes, and the lysosome. **(I)** Distribution of TbMyo1 in the cytoplasm and on subcellular structures. All gold particles 30 nm or closer to a structure were defined as being on the structure (based on a conservative calculation that two antibodies, each 15 nm in length, are between the bound epitope and the gold particle). More than half of the gold particles were found to be cytoplasmic. The total number of cells and gold particles quantified is indicated. Abbreviations: axoneme (Ax), flagellum (F), flagellar pocket (FP), plasma membrane (PM), nucleus (N). Exemplary single- and double-labelled images were chosen from three separate labelling experiments.

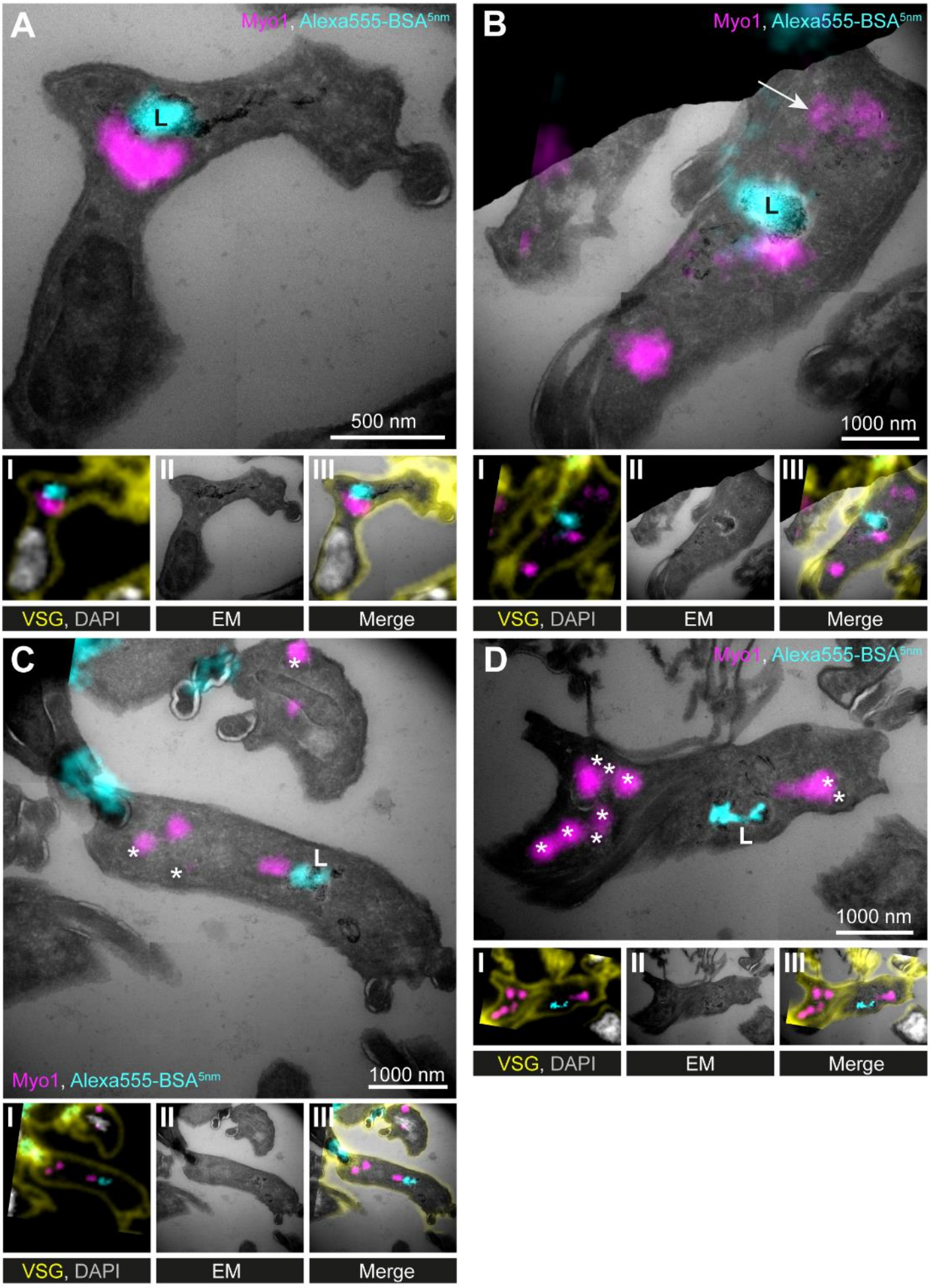
A
Myo1, Alexa555-BSA5nm
L
500 nm
I
II
III
VSG, DAPI
EM
Merge
B
Myo1, Alexa555-BSA5nm
L
1000 nm
I
II
III
VSG, DAPI
EM
Merge
C
L
Myo1, Alexa555-BSA5nm
1000 nm
I
II
III
VSG, DAPI
EM
Merge
D
Myo1, Alexa555-BSA5nm
L
1000 nm
I
II
III
VSG, DAPI
EM
Merge

Figure 5. TbMyo1 is clustered adjacent to the lysosome. (**A - D)** Correlative light and electron microscopy (CLEM) imaging of cryosections. To visualise cargo trafficking, cells were incubated with double-labelled Alexa555- and 5 nm gold-conjugated BSA (cyan) before fixation. Cryosections were labelled with anti-TbMyo1 (magenta), anti-VSG (yellow), and DAPI (grey). For each panel an image of the widefield microscopy **(I)**, the electron micrograph **(II)** and an overlay of both images **(III)** is presented. The electron micrographs are manually-stitched mosaics composed of multiple (4 – 9) tiled images of higher magnification (15,000x – 25,000x). Note that a fluorescence signal could only be detected at high local concentrations of Alexa555-BSA-5 nm gold. VSG and DAPI signals were used as fiducials to correlate IF and EM images. Correlations were made using the ec-CLEM plug-in in Icy for the initial correlation and Adobe Photoshop for the final overlay. Abbreviations: L – lysosome, * - glycosomes; the arrow in panel B shows endosomal tubes filled with BSA gold and positive for TbMyo1. Images show exemplary images from a sample of 17 correlated cells.

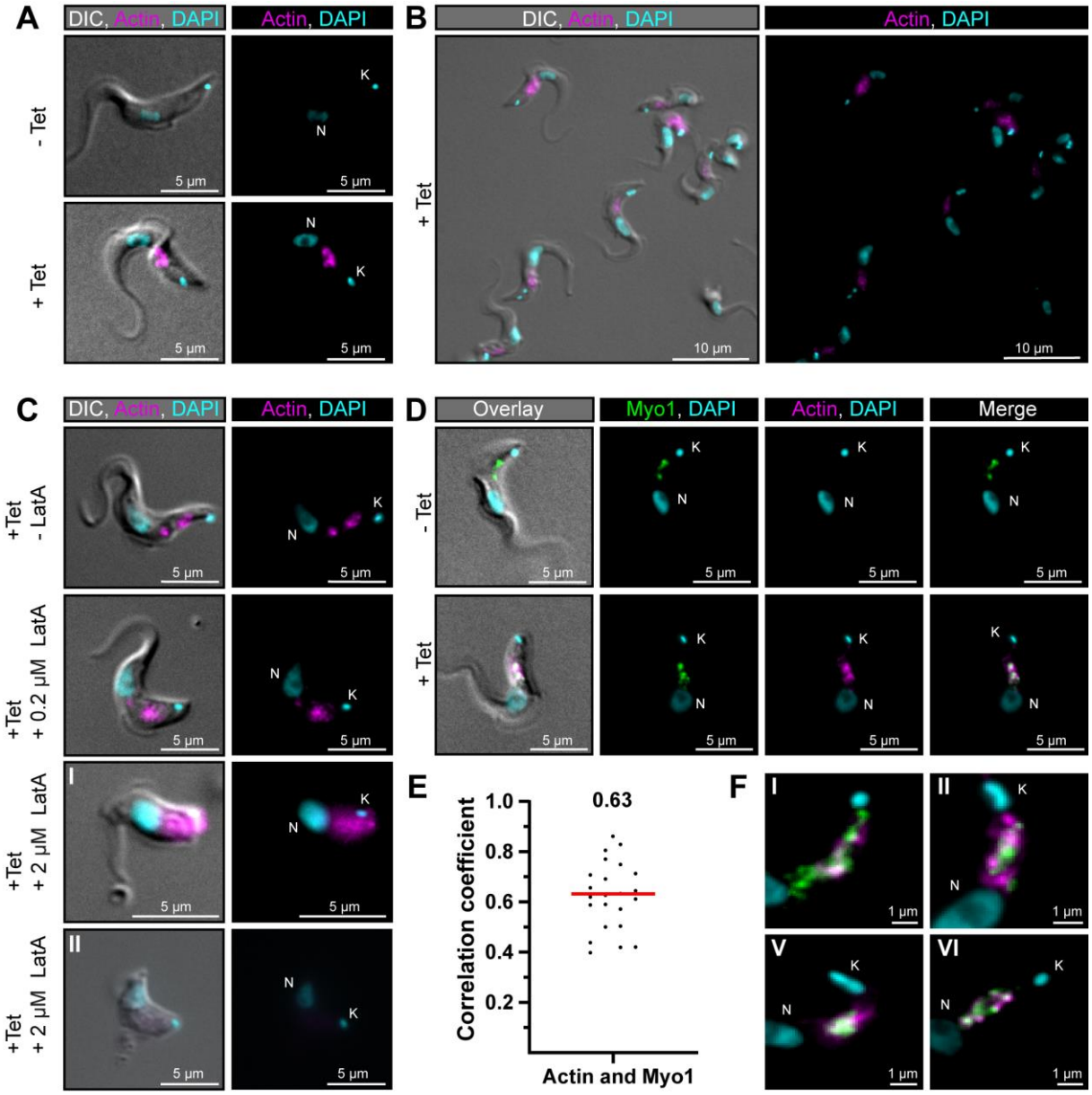

Figure 6. TbMyo1 overlaps extensively but not completely with actin. (**A)** Imaging of trypanosome actin using an inducibly-expressed anti-actin chromobody. Tetracycline (Tet) was used to induce expression of the anti-actin chromobody. Widefield microscopy of fixed cells in the absence (- Tet) or presence (+ Tet) of tetracycline are shown. The induced (+ Tet) cells showed a chromobody signal (magenta) in the posterior region of the cell between the nucleus (N) and kinetoplast (K), consistent with the reported localisation of actin in BSF *T. brucei*. DNA was stained with DAPI. **(B)** Cell-to-cell variation of the chromobody signal in the tetracycline-induced population. The intensity but not the distribution of the signal varied from cell to cell. **(C)** The actin depolymerising drug latrunculin A (LatA) disrupts the chromobody signal. Widefield microscopy of fixed, induced chromobody cells in the presence of different LatA concentrations. The cells in the absence of LatA (- LatA) acted as controls. The addition of 0.2 µM LatA led to a slight blurring of the chromobody signal (magenta), while 2 µM LatA resulted in strong blurring (**I**) or even loss of signal (**II**) accompanied by a disruption of cell morphology. **(D)** TbMyo1 strongly overlaps with the anti-actin chromobody signal. Non-induced cells acted as a control and showed no chromobody signal, with only a TbMyo1 signal (green). Induced cells displayed both a chromobody (magenta) and a TbMyo1 signal, which strongly overlapped in the posterior region of the cell. **(E)** Quantification of correlation between TbMyo1 and actin signals. Correlation was estimated using Spearman's rank correlation (n = 23). The median r is represented by a red line and the corresponding number is written above the data plot. **(F)** Enlarged view of the strong overlap between TbMyo1 and anti-actin chromobodies in the posterior region of the cell. Magnified images of the posterior region of four different cells (**I – IV**) are shown. TbMyo1 and the anti-actin chromobodies strongly overlapped in all cells examined, but the number and intensity of discrete spots varied.

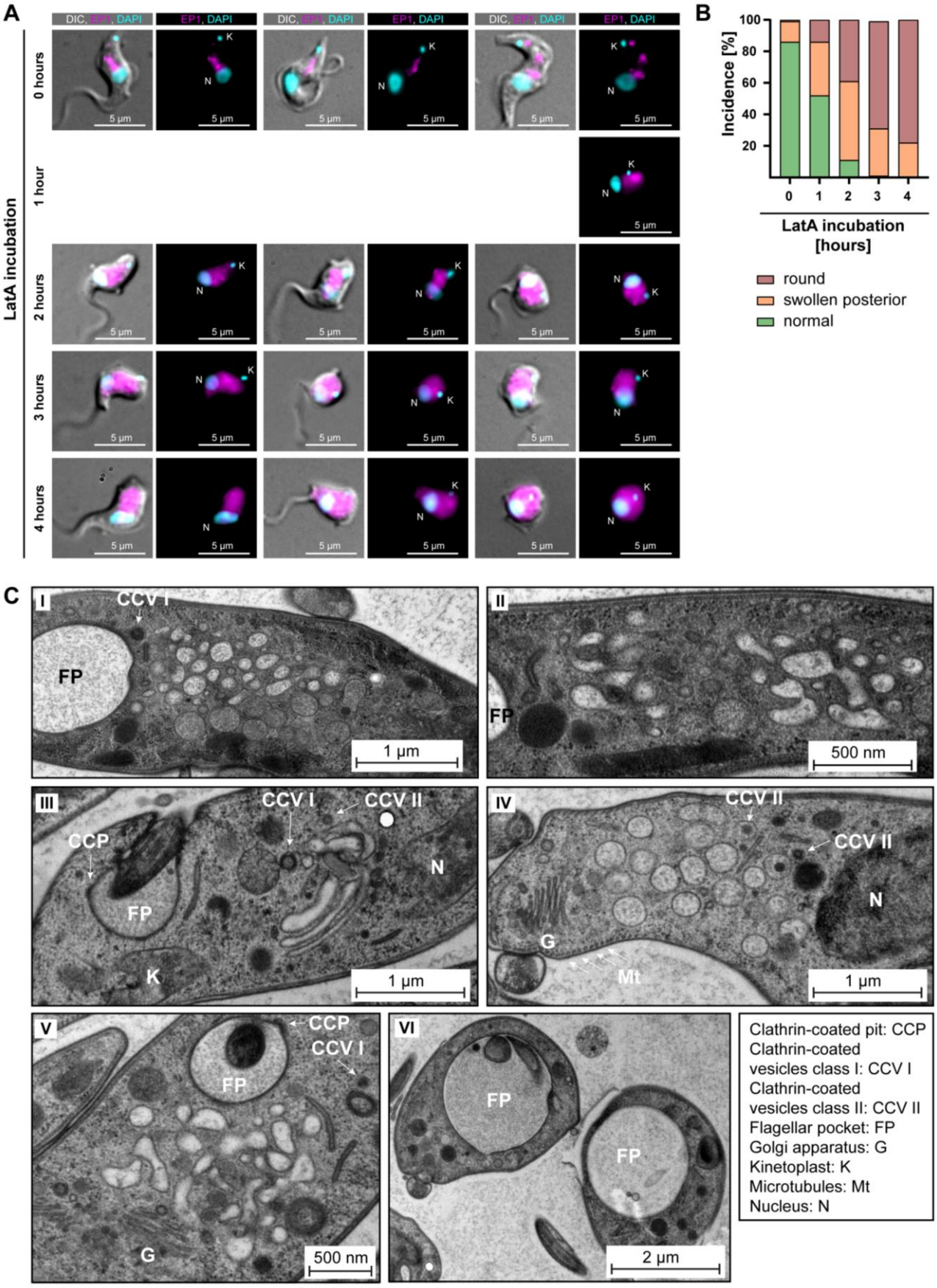
A
DIC, EP1, DAPI
EP1, DAPI
LatA incubation
0 hours
1 hour
2 hours
3 hours
4 hours
K
N
5 µm
B
Incidence [%]
100
80
60
40
20
0
1
2
3
4
LatA incubation [hours]
round
swollen posterior
normal
C
I
CCV I
FP
1 µm
II
FP
500 nm
III
CCV I
CCV II
CCP
FP
N
K
1 µm
IV
CCV II
CCV II
N
G
Mt
1 µm
V
CCP
CCV I
FP
G
500 nm
VI
FP
FP
2 µm
Clathrin-coated pit: CCP
Clathrin-coated vesicles class I: CCV I
Clathrin-coated vesicles class II: CCV II
Flagellar pocket: FP
Golgi apparatus: G
Kinetoplast: K
Microtubules: Mt
Nucleus: N

Figure 7. Actin depolymerisation disrupts the endosomal system. (A) LatA treatment perturbs the endosomal system. EP1-GFP expressing cells were incubated with 2 μM LatA for the indicated time periods, then fixed and imaged using widefield microscopy. DNA was stained using DAPI. Longer incubation with LatA resulted in aberrant cell morphologies and an increasingly diffuse EP1-GFP signal. Exemplary cells from a single experiment are shown. (B) Quantification of the morphological effects of LatA treatment. Cells were manually classified as displaying normal, swollen posterior, or rounded morphology. The degree of morphological disruption was proportional to the duration of incubation with LatA. Data acquired from >200 cells assayed in three independent experiments. **(C)** LatA treatment disrupts the ultrastructural morphology of the endosomal system. Cells expressing EP1-GFP were subjected to a 30 – 60 minute incubation with 2 μM LatA, followed by high-pressure freezing, embedding in Epon, and examination through transmission electron microscopy. The cytoplasm contained many large and interconnected tubular profiles, consistent with a swollen endosomal system. An enlargement of the flagellar pocket was additionally observed. Exemplary cells from a single experiment are shown.